Luminescent Sensing Platforms Based on Lanthanide Metal-organic Frameworks: Current Strategies and Perspectives

Xinrui Wang, Yupeng Jiang, Antoine Tissot, Christian Serre

Luminescent Sensing Platforms Based on Lanthanide Metal-organic Frameworks: Current Strategies and Perspectives

Xinrui Wang[a], Yupeng Jiang[b], Antoine Tissot[a,], Christian Serre[a,*]*

[a]*Institut des Matériaux Poreux de Paris, Ecole Normale Supérieure, ESPCI Paris, CNRS, PSL University, 75005 Paris, France*
[b]*Tianjin Key Laboratory of Structure and Performance for Functional Molecule, College of Chemistry, Tianjin Normal University, 393 Binshui West Road, Tianjin 300387, PR China*

ARTICLE INFO

Article history:
Received 00 December 00
Received in revised form 00 January 00
Accepted 00 February 00

Keywords:
Lanthanide Metal-organic Frameworks (Ln-MOF), Luminescence

ABSTRACT

Lanthanide metal-organic frameworks (Ln-MOFs) have aroused increasing interest due to their highly effective luminescence from their constitutive metal ions, ligands, and/or the inserted or absorbed guests, enabling a good luminescence response in analysis. This review aims to present a thorough understanding of the design principles of Ln-MOFs and the associated detection mechanisms. Sensors utilizing Ln-MOFs are categorized into three distinctive classes, distinguished by diverse synthesis strategies: Monometallic lanthanide MOFs, MOFs with intrinsic dual-emission properties, and innovative Ln-MOFs composites. Within each section, we explain the design strategies employed and the associated corresponding merits. Additionally, the review concludes with a presentation of the numerous applications where Ln-MOFs based luminescent sensors had a significant impact.

Contents

1. Introduction

Metal-organic frameworks (MOFs) are crystalline hybrid materials formed with metal ions[1], oxoclusters[2], chains or layers[3], and polydentate ligands linked through coordination bonds[4]. MOFs present a high potential for applications in adsorption[5], separation[6], energy storage[7-9], catalysis[10-12], drug delivery[13-15], sensing[16-20], electrochemistry[21-23], etc., due to their highly tunable chemical and structural features associated with multidimensional micro or mesoporous structures with various functional groups[24-28]. Lanthanide metal-organic frameworks (Ln-MOFs) have characteristic intrinsic luminescent properties[29] such as light emission covers a wide spectral range from ultraviolet to NIR. Ln-MOFs have been investigated in optical fields such as sensing[30-33], LED lighting[34], and medicine[35]. Especially, Ln-MOFs have bloomed in the sensing area in the last decades because they possess highly stable and adjustable luminescence emission signals, high quantum yield, and long lifetime. These merits lead to high sensitivity, simple operation, and short response time during the detection process. In addition, most Ln-MOFs can be easily synthesized through a one-pot route[36] (Scheme 1). Ln-MOFs' optical performances can be tuned by the choice of lanthanide (or mixtures of lanthanides) ions and organic ligands, which can lead to the formation of highly porous structures or provide additional chromophores in the solid (Scheme 1). These organic ligands usually provide multiple oxygens and nitrogen-containing coordination environments while the aromatic spacer enables an efficient optical absorption.

Laporte's rule typically limits the excitation of lanthanide ions, as the 4f-4f transitions are forbidden[37]. However, a suitable "antenna" can significantly sensitize lanthanide ions through ligand-to-metal energy transfer (LMCT) processes[38]. Consequently, some Ln-MOFs can emit dazzling light under ultraviolet light excitation such as Eu-MOFs (red light) and Tb-MOFs (green light). In addition, the characteristic emission of Yb-MOFs, Nd-MOFs, and Er-MOFs in the near-infrared region has also

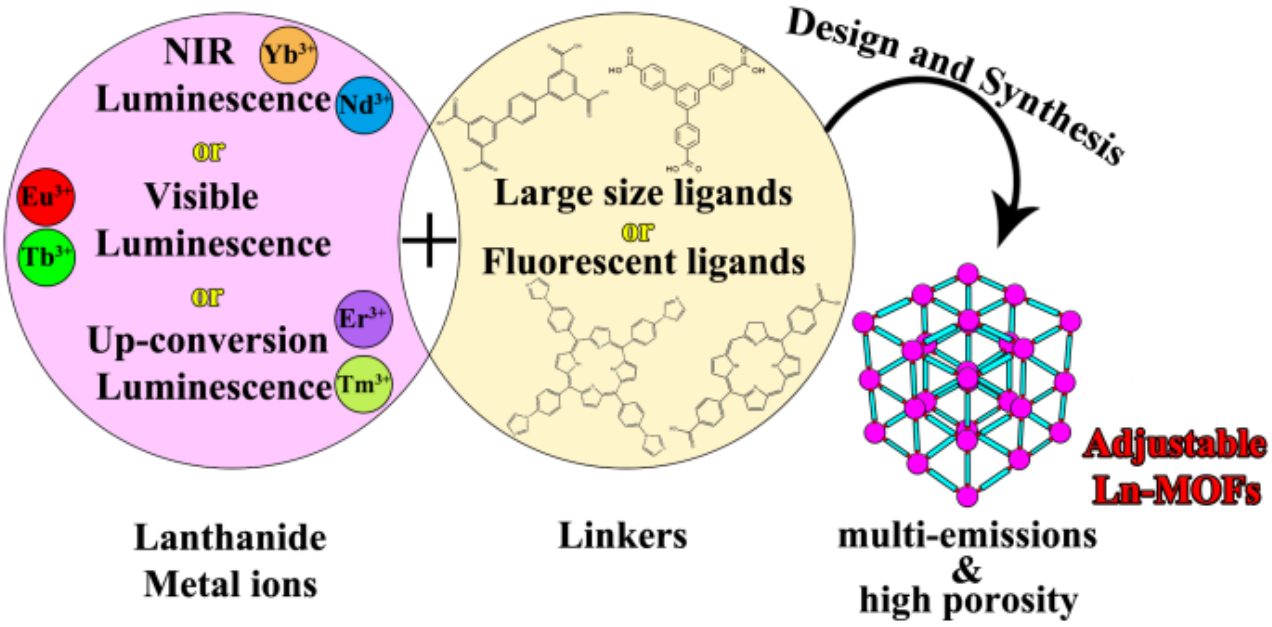

Scheme 1. Illustration of the synthetic strategy of Ln-MOFs

attracted great attention[39, 40]. Recently, up-conversion emission from near-infrared excitation light into visible light has been observed with some bimetallic Ln-MOFs, such as Gd/Tm-MOFs(1), Yb/Tm-MOFs(2), and Yb/Er-MOFs(3)[41], that therefore present great potential in photocatalysis, biomolecular recognition, etc.

Mono- or bi-metallic lanthanide MOFs are known for their excellent luminescent properties[42]. Additionally, composites based on lanthanide MOFs have also shown impressive optical features. For example, Ln-MOF-based composites can accommodate optically active guest molecules relying either on their intrinsic porosity, defects, or active functional groups, leading to enhanced luminescent properties suitable to construct ratiometric fluorescent sensors. Furthermore, Ln-MOFs can be functionalized by introducing specific functional groups either inside the pores or at the external surface to interact with larger molecules (chromophores, DNA/RNA sequence, chiral molecules, etc.). In addition, to further enhance the sensitivity of Ln-MOFs and/or improve the signal stability, one can decrease their particle size to the nanoscale. Thus, one can envision preparing specific functional Ln-MOFs-based materials to form highly sensitive detection for special purposes, especially focusing on multifunctional sensing.

In comparison with previous works [43, 44] mainly focused on pure Ln-MOF, this work gives more insights on Ln-MOF based composites and discusses several methods to identify combination modes between Ln-MOF and guest molecules. Additionally, given the need for comprehensive reviews encompassing the different detection strategies, especially for turn-on systems, this review describes design strategies, detection mechanisms, and recent applications of Ln-MOFs based materials to show their potentiality, especially for time-resolved technologies and time-gated detection techniques. In addition, perspectives on the future of Ln-MOFs based multifunctional sensors are presented.

2. Synthesis and structure of Ln-MOFs

Highly crystalline Ln-MOFs are prepared using hydrothermal or solvothermal methods in most cases, in which the synthesis process usually implies high temperature and high pressure[45-47]. Factors affecting the formation of Ln-MOFs include temperature, pressure, pH, the concentration of metals and ligands, etc[48-51]. Organic acids can be used as modulators, and in some cases, the use of formic acid, acetic acid, trifluoroacetic acid, etc. is beneficial to obtain single crystals of Ln-MOFs [52, 53]. The synthesis time of Ln-MOFs ranges from several hours to several days and can also influence crystal crystallinity and particle size[54, 55]. The first example of large pores water-stable MOF was reported by some of us using a cyclohexanol/water mixture under solvothermal conditions. Its structure is built from the BTB ligand delimiting large 1 nm channels paved with open metal sites, leading to high surface area exceeding 930 $m^2.g^{-1}$[56]. Recently, Wiwasuku et al. synthesized another water-stable 3D Tb-MOF(4) under solvothermal conditions[57] by mixing H_4BTEC and $Tb(NO_3)_3$ in deionized water and then heating the solution in an oven at 120 °C for 12 h. Under excitation at 254 or 280 nm, the MOF has excellent green characteristic luminescence and can be used for ultra-low detection limit detection of paraquat. However, solvothermal and hydrothermal methods usually require a long synthesis time. Recently, electrochemical, ultrasonic, and microwave syntheses became more popular[58] thanks to their fast and controllable processes[59]. For example, Cao et al[60]. reported the preparation of microporous Ln-MOFs via microwave-assisted solvothermal reaction. This led to a significant reduction of the synthesis time from 5 h (solvothermal) to 5 min and provides an ideal route for the large-scale production of Ln-MOFs.

The diversity of organic ligands determines the variety of Ln-MOF's structures and in general, Ln-MOFs constructed with large ligands exhibit larger pores. For example, the MOF-76 (Ho/Tm) (5) reported by Almáši et al. uses BTC as the organic ligand[61]. MOF-76 (Ho) and MOF-76 (Tm) exhibit the same structure delimiting one-dimensional channel of about 6.7 × 6.7 $Å^2$, associated with BET surface areas of 600 $m^2\ g^{-1}$ and 590 $m^2\ g^{-1}$, respectively. However, when the organic ligand was replaced by BTB, as explained above, this leads to the MIL-103 (Tb) (6) with large micropores and a higher BET surface area[56]. Therefore, the selected organic ligand plays an important role in enhancing the emission of Ln-MOF through the antenna effect. As shown in Scheme 2, the organic ligands used in synthesizing Ln-MOF

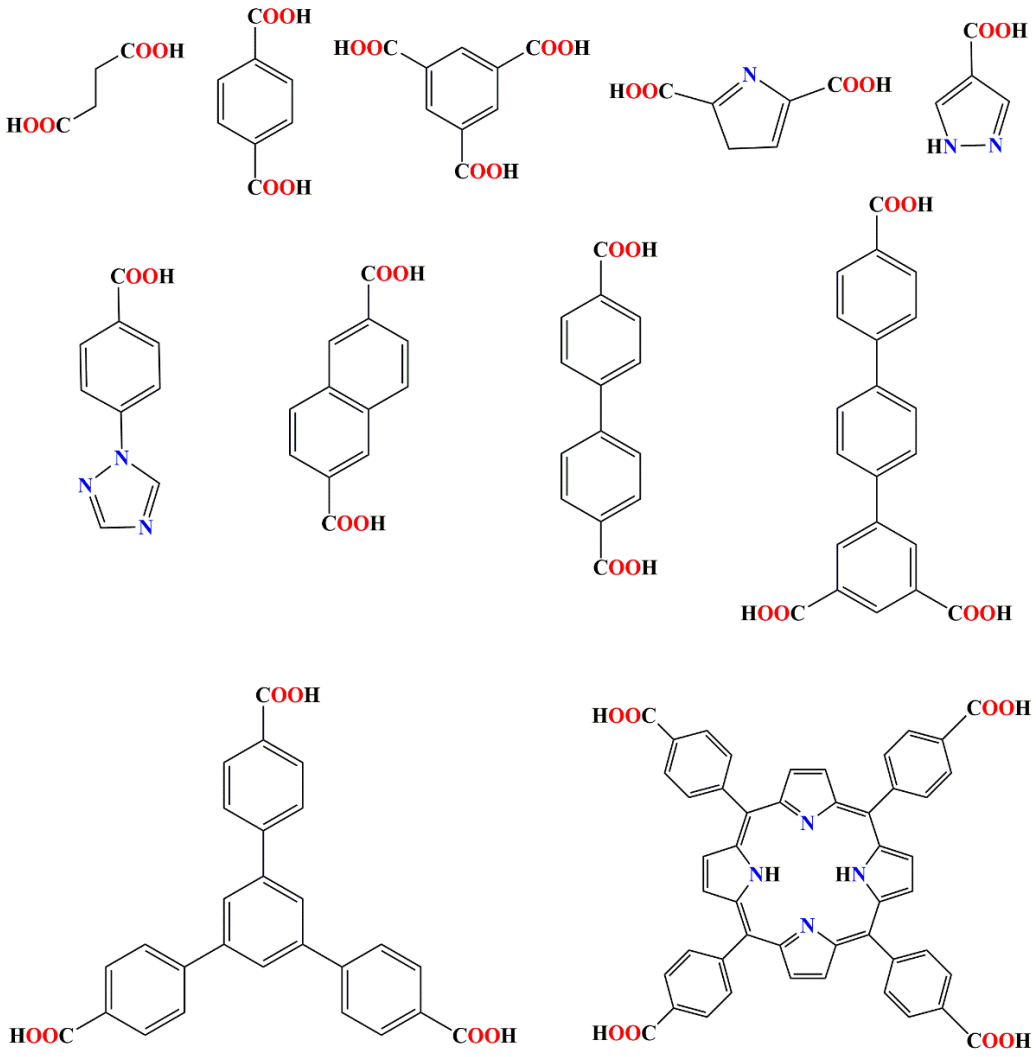

Scheme 2. Examples of organic ligands used to synthesize Ln-MOFs.

include polycarboxylic acids, diazoles, triazoles, etc. In the down-conversion emission process, the lanthanides in Ln-MOF primarily exist in the trivalent state $\{Ln^{3+}: [Xe]4f^n$ $(0 < n < 14)$, thereby exhibiting remarkable photostability. Additionally, their distinct 4f-4f transitions result in well-defined luminescence spectra encompassing a wide range of wavelengths, from UV to near-infrared (NIR). For example, the Ce^{3+} ion exhibits a broad UV emission (5d-4f transition) spanning 370 to 410 nm. Moving into the visible spectrum, the Eu^{3+}, Tb^{3+}, Sm^{3+}, and Tm^{3+} ions emit red, green, orange, and blue luminescence, respectively. The NIR emission luminescence is obtainable with Nd^{3+}, Yb^{3+}, Pr^{3+}, Er^{3+}, and Ho^{3+} ions. For up-conversion processes, NIR lasers (for instance, at 980 nm and 808 nm) can excite Er^{3+} and Nd^{3+}, resulting in visible emission.

Lanthanides with different ionic radii exhibit distinct coordination numbers (8 or 9 in the most of examples in Ln-MOF). Consequently, the energy associated with the $4f^{n-1}5d^1$ configuration within Ln-MOF lattices experiences a gradual decrease as the number of electrons within the f-orbital ranges from 1 to 14. This phenomenon can be attributed to the diminished interaction between the occupied 4f subshell (populated by $4d^{10}$ electrons) and the neighboring coordinated organic ligands or solvent molecules. As an illustration, in a study by Abdelhamid et al[62], two lanthanide MOFs, namely SUMOF-7II(7) and SUMOF-7IIB(8), were synthesized utilizing H_3L_2 as ligand and H_3BTB as linkers. The MOFs presented a pore size of 11.3 Å and emit bright red light with a luminescence quantum yield (QD) of 4% for SUMOF-7II(Eu) and 5% for SUMOF-7IIB(Eu). The reason for such a difference is that in the H_3L_2 ligand, the central graphite ring is substituted with a pyridine ring, the latter possessing lone pair electrons on its N-atom and led to a different coordination mode and adjustable structure and therefore to higher quantum yield.

In summary, the diversity of structures and chemical properties of Ln-MOFs strongly affects their optical properties, and the porosity of the structures can be used to directly accommodate guest molecules in the pores to construct Ln-MOFs composites. Therefore, Ln-MOFs have recently attracted a lot of attention in research fields such as luminescence, sensing, imaging, and catalysis[63-66].

3. Photoluminescence mechanism

Coordination chemistry is critical in determining the photoluminescence properties of Ln-MOF. The coordinated mode of the lanthanide ion, which is the arrangement of atoms or ligands surrounding it, directly influences its energy levels and electronic configuration[67] and therefore, different coordination environments can lead to different

photoluminescence properties. For example, the presence of different ligands or substituents in the coordination sphere can significantly alter the energy levels of the lanthanide ions, leading to different PL properties[68]. Some illustration of this phenomenon can be found in Table 1.

Crystal structure and morphology also significantly impact the photoluminescence (PL) properties of Ln-MOFs[69]. The crystal structure influences the local environment of the lanthanide ions, leading to changes in their energy levels and electronic configuration. It can also affect the exciton diffusion length and the radiative and non-radiative decay rates, which can significantly modify the PL properties of Ln-MOFs. For example, the existence of unoccupied coordination sites in the framework can potentially improve the diffusion range of excitons and decrease the rate of non-radiative decay, thus leading to higher efficiency of photoluminescence[70].

Energy transfer mechanisms, such as ligand-to-metal charge transfer (LMCT) and ligand-ligand energy transfer (LLET), are crucial factors that affect the photoluminescence properties of Ln-MOFs[71]. The LMCT process involves the transfer of energy from the ligand's excited state to the lanthanide ion, while the LLET process pertains to the transfer of excited state energy within the ligand molecule (Scheme 3). The efficiency of energy transfer is influenced by the difference in energy levels between the excited state of the ligand and the energy levels of the lanthanide ions[72]. It is important to distinguish between different energy transfer processes, such as Förster energy transfer, Dexter energy transfer, and photoinduced

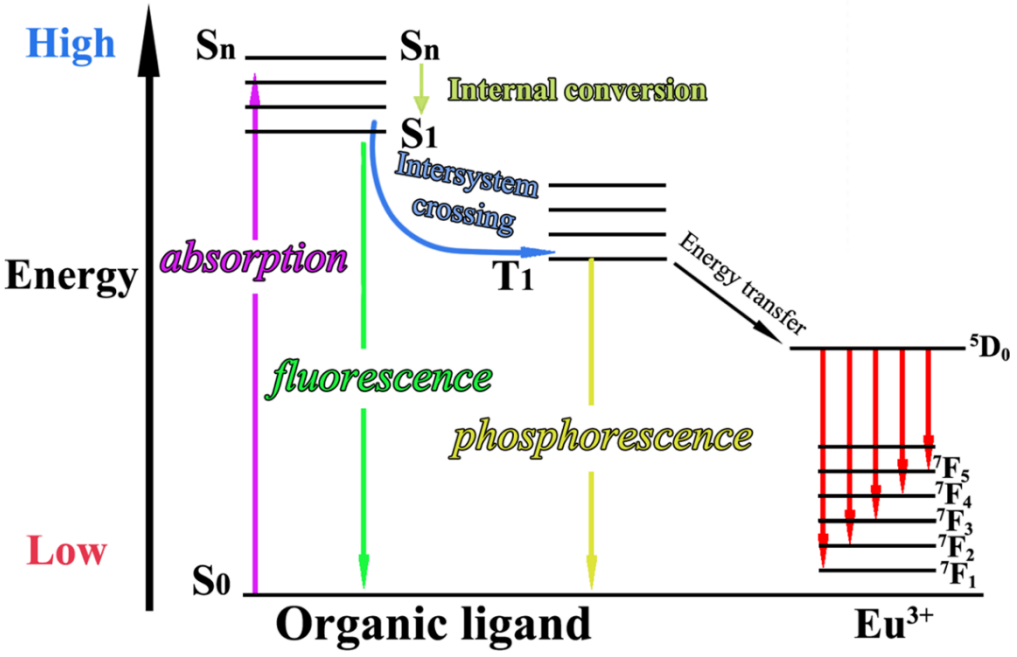

Scheme 3. Illustration of the different energy transfer processes in Eu-MOFs.

electron transfer (PET). According to the Förster energy transfer mechanism, the energy released from an excited donor molecule can be effectively transferred to a ground-state acceptor molecule through the Coulombic interaction between them. This process allows the acceptor to become excited simultaneously. In contrast, Dexter energy transfer involves the direct exchange of electrons between an excited donor group and an acceptor group, facilitating a non-radiative energy transfer pathway[73]. Dexter energy transfer, in contrast to the sixth-power dependence observed in Förster energy transfer, follows an exponential decay pattern for the reaction rate constant as the distance between the interacting entities increases. Due to this exponential relationship, the exchange mechanism predominantly takes place within a range of approximately 10 Å. Dexter exchange energy transfer is commonly associated with the phenomenon of quenching, which leads to a decrease in fluorescence intensity[74]. PET is an excited-state process in which an electron, initially in an excited state, is transferred from a donor molecule to an acceptor molecule. This electron transfer event leads to the creation of charge separation between the donor and acceptor species, thereby initiating a redox reaction within the excited state, in contrast with the Dexter energy transfer. In addition, polar solvents like water can cause a quenching effect in luminescence. This occurs because the solvent can adjust the energy difference between triplet and singlet states, increasing non-radiative relaxation processes. Similarly, intermolecular hydrogen bonding can have a profound impact on the electronic properties of the compounds, leading to red-shifts and blue-shifts that correspond to the strengthening and weakening of these interactions, respectively. The influence of hydrogen bonding on electronic states can also dramatically modulate radiationless deactivation pathways, such as internal conversion (IC), PET, intramolecular charge transfer (ICT), and metal-to-ligand charge transfer (MLCT). Consequently, the fluorescence behavior of chromophores in hydrogen-bonded environments can be modulated, leading to either quenching or enhancement of their fluorescence properties. Although Ln^{3+} ions are prone to quenching, it is possible to eliminate several quenching factors. For instance, the collapse of the Ln-MOF structure, identifiable through XRD analysis, and the agglomeration of Ln-MOF particles, observable via SEM, can be preemptively addressed. To ensure that quenching exclusively comes from the analyte, it is advisable to assess the emission stability of Ln-MOF using luminescence tests. To enhance optical transmittance and amplify luminescence signals, a promising approach involves synthesizing Ln-MOFs into nanoparticle sizes. This strategy not only bolsters luminescence by mitigating scattering losses but also achieves signal stability through the formation of a suspended MOF solution. Additionally, the combination of some guest molecules with Ln-MOFs can also work as a second antenna and further improve the energy transfer process between ligand and Ln^{3+} when there are spectral overlaps (absorption and emission spectra) between ligand and guest

molecules.

Computational chemistry can help in understanding and predicting the photoluminescence properties of Ln-MOFs[75]. Indeed, calculations can predict energy levels of lanthanide ions in different coordination environments and crystal structures, which can guide the design of Ln-MOFs with tailored photoluminescence properties. Additionally, calculations can be used to understand the energy transfer mechanisms involved in the photoluminescence process, providing insights into the factors that influence the photoluminescence properties of Ln-MOFs[76].

In conclusion, a deep understanding of coordination chemistry principles, crystal structure, and energy transfer mechanisms is essential in designing and synthesizing Ln-MOFs with improved photoluminescence properties[77, 78]. The interplay of these factors can be manipulated to tailor the photoluminescence properties of Ln-MOFs for various applications, including sensing, imaging, and optoelectronics. Computational chemistry is also a valuable tool to predict and understand the photoluminescence properties of Ln-MOFs and guide the development of new materials with tailored photoluminescence properties.

Table 1. Examples of different types of sensing mechanisms of Ln-MOFs-based luminescent sensor

Sensor name	Mechanism	Analyte	Excitation	Emission	Ref
Tb_nGd_{9-n} clusters (9)	Back energy transfer (BEnT)	Metronidazole, Picric acid	330 nm	545 nm	[79]
Eu^{3+}@UiO-bpydc (10)	Back energy transfer (BEnT)	Ascorbic acid	395 nm	530 nm, 614 nm	[80]
CUST-507 (11)	Dynamic quenching effect	Metronidazole,Picricacid	285 nm	405 nm, 614 nm	[81]
$Eu_{0.7}Gd_{0.3}$-tfBDC-MOF (12)	Dynamic quenching effect	Ascorbic acid	330 nm	614 nm, 415 nm	[82]
$[Eu_2IJtcptp)IJbtca)IJH_2O)_m]_n$ (13)	Energy transfer	Nitrofurantoin, levofloxacin	330 nm	616 nm	[83]
$[Eu(atpt)_{1.5}(phen)(H_2O)]_n$(EuMOF) (14)	Competitive absorption	N-acetylneuraminic acid	356 nm	470 nm, 614 nm	[84]
Gd/Tm-MOFs@$mSiO_2$-FA (15)	Excited state absorption (ESA)				[85]
Up-MOF-Y/Er (16)	Excited state absorption (ESA)		980 nm	540 nm	[86]
Tb/Eu-PGO-COOH (17)	Inner filter effect (IFE)	2,4-dinitrotoluene (DNT)	253.7 nm	545 nm, 615 nm	[87]
Cu/Tb@Zn-MOF (18)	LMCT	aspartic acid	365 nm	546 nm	[88]
GOx-Eu^{3+}@UMOF (19)	Energy transfer	glucose	310 nm	614 nm	[89]
Tb^{3+}@Cu-MOF (20)	MLCT	H_2S	280 nm	390 nm, 544 nm	[90]
RBH@Eu(BTC) (21)	FRET	picric acid	281 nm	353 nm, 530 nm	[91]
RhB@HNU-48 (22)	Competition absorption, energy transfer, and electron transfer	Alachlor	370 nm	470 nm, 585 nm	[92]
Cu–Eu MOFs/Cu–Tb-MOFs (23)	Exciplex between Cu–Eu-MOFs and 6-MP/6-TG	6-MP and 6-TG	340 nm	470 nm, 613 nm	[93]
Ln-BPTA (Eu, Sm, Dy and Tb) (24)	FRET	Riboflavin	320 nm	530 nm, 446 nm, 380 nm	[94]
$[Eu(ADA)_{1.5}$ (phen)$]_n$ (25)	LMCT	Ni^{2+}	345 nm	592 nm	[95]
Tb-PTC, Tb-BPTC, and Tb-TPTC (26)	Anion-Π interaction and Anion−cation electrostatic interaction	Alkaline phosphatase	275 nm	420 nm, 552 nm	[96]
$\{[Ln(dpc)(2H_2O)]\cdot(Hbibp)_{0.5}\}_n$ (27)	Energy transfer	Fe^{3+}, Cu^{2+}, $Cr_2O_7^{2-}$	339 nm	616 nm	[97]
$\{La_{0.88}Eu_{0.02}Tb_{0.1}(DCBBA)(DMF)_2]_n\cdot H_2O\cdot 0.5DMF\}_n$ (28)	Hydrogen bonding	THF	300 nm	616 nm	[98]
$Eu_2(sbdc)_3(H_2O)_3$ (Eu-sbdc) (29)	Dynamic or static quenching processes, spectral overlap, or energy transfer,	Adenosine triphosphate	335 nm	618 nm	[99]
Tb-PTA-OH (30)	Direct sensitization and indirect sensitization pathway	Dipicolinic acid	275 nm	436 nm, 455 nm	[100]
$[Eu_2IJtcptp)IJbtca)IJH_2O)_m]_n$ (31)	Energy transfer	Nitrofurantoin, levofloxacin	330 nm	616 nm	[101]

4. Monometallic lanthanide MOFs sensors

Single-metal Ln-MOFs have been utilized as luminescence sensors for detecting metal ions, anions, small organic molecules, and nitro explosives [102-105]. To optimize the detection of these target molecules, three main types of luminescence modification strategies have been proposed: enhancement, quenching, and dual-emission self-calibrating detection [106-108]. In 'turn on' detection, the analyte can enhance the luminescence of Ln-MOF, typically accompanied by energy transfer from the analyte to the Ln-MOF. The quenching mechanism is typically associated with the interaction between the analyte and Ln-MOF, along with energy transfer from Ln-MOF to the analyte[109]. Dual emission self-calibration detection usually occurs in the case where both the ligand and the lanthanide metal present a characteristic emission and can be subdivided into two categories. The first one is that the dual emission peaks are simultaneously quenched or enhanced under the influence of the analyte but to different degrees. The second type corresponds to one enhanced peak while the second one is simultaneously quenched.

Bu's group[110] introduced a novel Eu-MOF featuring Eu_9 clusters with unoccupied coordination sites. These open metal sites created an enclosed "binding pocket" ideal for efficient preconcentration and

identification of volatile organic compound (VOC) vapors. Capitalizing on the high Eu^{3+} luminescence, the MOF achieves real-time, on-the-spot sensing of THF vapor in less than one second. Additionally, it exhibits a precise ratiometric response to vapor pressure, reaching a detection limit as low as 17.33 Pa.

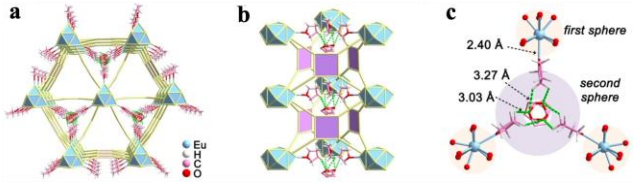

Fig. 1. Structure of NKU-200-Eu@THF obtained by single-crystal diffraction (a) Overhead and (b) lateral perspectives of THF molecule encapsulation within NKU-200-Eu's 1D open channel. (c) Depiction of interactions within NKU-200-Eu@THF, encompassing the first and second coordination spheres. [110] Copyright 2023, Wiley-VCH Verlag.

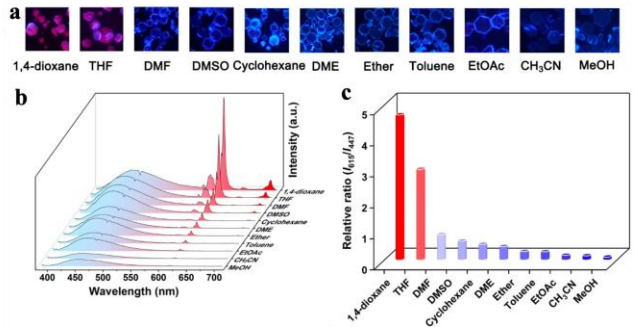

Fig. 2: (a) luminescence images of NKU-200-Eu-solvents' response to various solvents under 365 nm UV excitation. (b) Spectra of luminescence emissions and (c) the intensity ratio (I_{615}/I_{447}) across the spectrum for NKU-200-Eu's solvent-inclusion crystals (λ_{ex}=365 nm). [110] Copyright 2023, Wiley-VCH Verlag.

In-depth analyses using SCXRD were performed on single crystals containing solvent inclusions. Leveraging the presence of a "binding pocket," the channel's aperture selectively captures and accommodates unbound molecules of THF. These guest molecules coordinate with Eu_9 clusters by competitively displacing three equatorial H_2O ligands. The coordinated inclusion of these analytes serves a dual purpose. Firstly, it shields OH quenchers from the first coordination sphere of Eu^{3+}. Secondly, it establishes a spatial confinement that allows potential interaction with uncoordinated molecules (Fig 1a-1b). Its stability is maintained by the presence of the three coordinated molecules, forming C-H···O bonds at distances measuring 3.03 and 3.27 Å (Fig 1c). When exposed to a 365 nm UV lamp, the majority of solvent-inclusion crystals emit blue fluorescence. Notably, NKU-200-Eu@THF (32) deviate from this pattern, displaying a magenta emission associated to more intense Eu^{3+} luminescence (Fig 2a). Solid-state emission spectra further reveals that the inclusion of distinct solvents results in discernible ratiometric luminescence responses. This observation highlights the crucial role of the solvents used in affecting the luminescence intensity of NKU-200-Eu (as depicted in Fig 2b-2c, indicating that NKU-200-Eu possesses the ability to selectively detect 1,4-dioxane and THF.

Qu et al[111]. reported another example of a luminescent probe using a novel boronic acid (BA) functionalized Europium MOF (BA-Eu-MOF) (33) to detect Hg^{2+} and CH_3Hg^+ ions. The MOF is built with 5-bromobenzene-1,3-dicarboxylic acid (5-bop) as ligand, which provides an active site for the targeted analytes. However, the strong electron-withdrawing effect of BA group weakened the antenna effect of BA-Eu-MOF, resulting in only weak red-light emission in water, much weaker than that of strongly emitting MOFs such as Eu-BTB. Upon addition of different concentrations of Hg^{2+} and CH_3Hg^+ ions to the MOF aqueous solution, the red luminescence of BA-Eu-MOF was greatly restored due to the specific interaction between the ions and the BA-Eu-MOF (Fig. 3). Furthermore, adding other metal ions to the solution did not affect the red emission of BA-Eu-MOF. In this example, BA weakens the energy transfer to Eu^{3+} in the BA-Eu-MOF, but the chemical reaction between BA and the detection substrate promotes the characteristic luminescence of the MOF (Fig. 4). This approach demonstrates how a specific chemical reaction between the sensor and detection substrate can affect the energy transfer mechanism and successfully design a discrimination strategy. Future work could explore if BA-Eu-MOF is capable of discriminating Hg^{2+} and CH_3Hg^+ in a mixture solution. In addition, one also need to consider whether the material can be recycled.

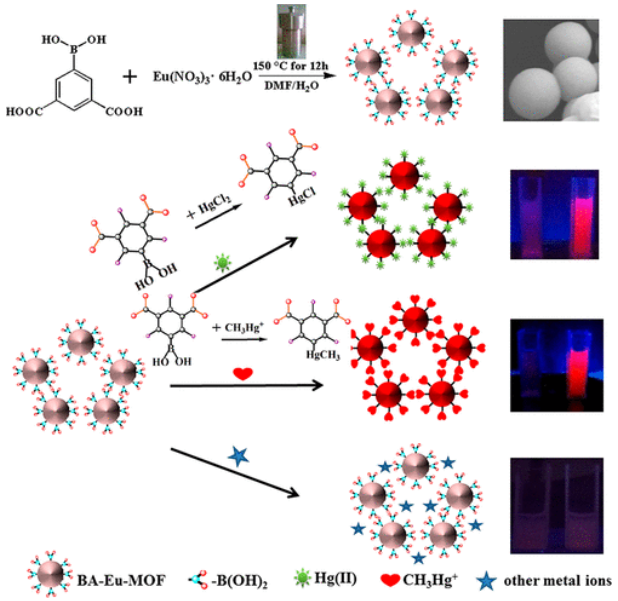

Fig. 3. Synthesis route of BA-Eu-MOF and its emission towards Hg^{2+} and CH_3Hg^+ ions through linker modification. [111] Copyright 2020, American Chemical Society.

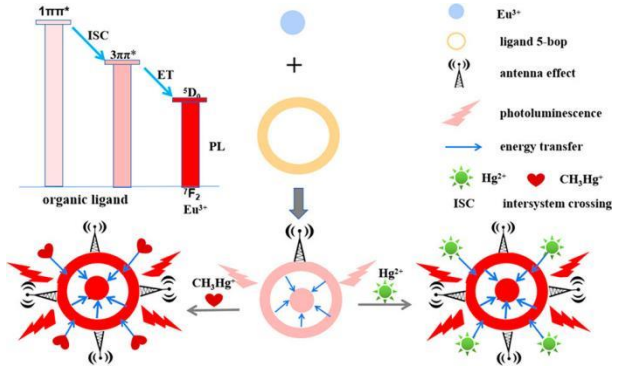

Fig. 4. Sensing mechanism of ligand-metal energy transfer progress and enhanced "antenna" effect caused by Hg^{2+} and CH_3Hg^+ ions. [111] Copyright 2020, American Chemical Society.

Ma et al[112]. reported another example of a Tb(III)-based MOF (MMCF-4) (34) for the sensing of methylamine. MMCF-4 exhibited a super-low limit of detection (LOD) and was employed a turn-on system. The MMCF-4 structure includes a secondary coordination sphere dominated by dense hydrogen-bonding interactions that promote long-range interactions between the analyte and MOF (Fig. 5). SCXRD and calculations confirmed the combination mode of analyte@MMCF-4 and the MMCF-4 structure, suggesting why the analyte enhanced the luminescence of MMCF-4 through a turn-on system (Fig. 6). This work could be completed by the investigation of the luminescent response of MMCF-4 after adding other analytes which possess a similar structure with methylamine and 6-mercaptopurine.

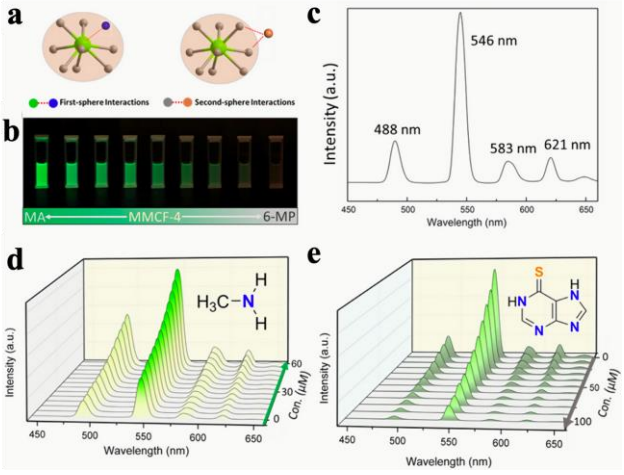

Fig. 5. (a) Diagram illustrating the interactions between the first and second coordination spheres in MMCF-4; (b) Photographic images of MMCF-4 under 260 nm UV light with different concentrations of MA/6-MP; (c) Luminescence spectrum of MMCF-4 after added of (d) methyl amine and (e) 6-mercaptopurine. [112] Copyright 2021, Wiley-VCH Verlag.

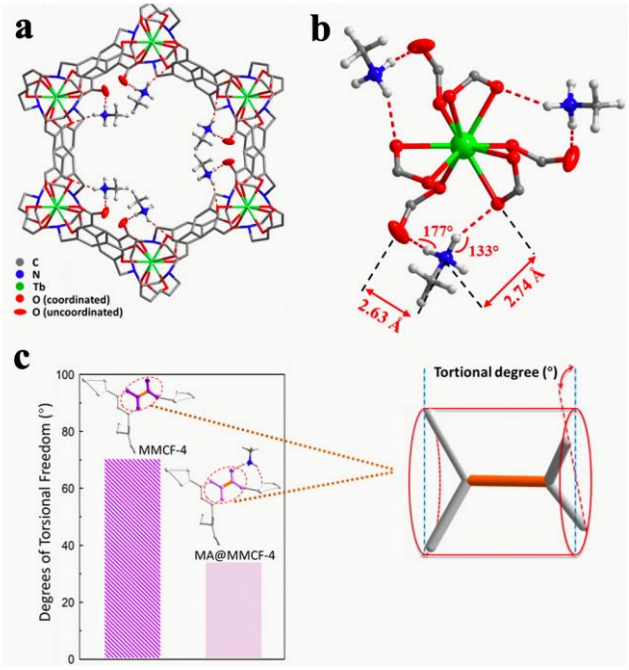

Fig. 6. (a) Structure of MA@MMCF-4 evidencing the methyl amine guest molecules inside the pores; (b) the interactions between methyl amine and Tb oxocluster. (c) Degrees of torsional freedom for ligand in MMCF-4 and MA@MMCF-4. [112] Copyright 2021, Wiley-VCH Verlag.

In the case of "turn off" sensing, Li et al[113]. reported an Eu-MOF (35), synthesized from Eu^{3+} and H_2NDC under solvothermal conditions. The acidity of the solution was shown to impact the luminescence of this MOF: when the pH of the aqueous solution was higher than 4, it showed a red luminescence under ultraviolet light excitation, while when the pH was lower than 3, it showed blue luminescence (Fig. 7). The pH control switch was attributed to a change of terminal coordinated solvent molecules, as shown by the study of the conversion from single crystal to single crystal (SC-SC) that evidenced subtly varies in the Eu-O bonds, which affected the antenna effect and reduced the ligand-to-metal energy transfer efficiency at pH below 3.

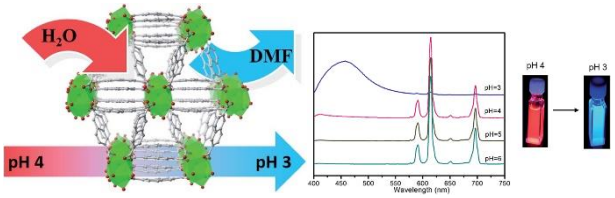

Fig. 7. Structure and luminescence spectra of Eu-NDC in response to pH modulation. Photographs of Eu-NDC under 365 nm UV light when subjected to pH 4 and 3. [113] Copyright 2019, Royal Society of Chemistry.

Based on short-range pH sensing switch characteristics of this MOF, the authors exploited it to detect traces of aspartic (Asp) and glutamic (Glu) acids in an aqueous solution (Fig. 8). During the detection process, the characteristic emission peaks of Eu-MOF were gradually quenched upon exposure to different concentrations of substrates. This was associated with a gradual increase emission of ligand, attributed to gradually low pH upon the addition of analytes.

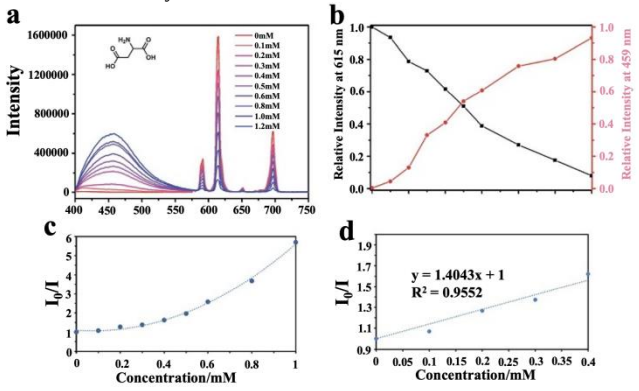

Fig. 8. (a) Emission spectra of Eu-NDC measured in aqueous solutions containing varying concentrations of Asp; (b) Relationship between Asp concentration and relative intensity measured at 615 nm and 459 nm; (c) Stern-Volmer (S-V) plot of Eu-NDC in the presence of Asp; (d) Linear regression analysis of the luminescence spectra of Eu-NDC in the presence of low concentrations of Asp. [113] Copyright 2019, Royal Society of Chemistry.

5. Bimetallic-based Ln-MOFs

Lanthanide ions exhibit similar chemical properties, and thus can present similar coordination modes within the same MOF structure[114].

Therefore, in each Ln-MOF, it is usually very easy to simultaneously introduce multiple lanthanide metals to construct multi-emission MOFs[115, 116] that are single-phase solids (not a physical mixture of several phases)[117]. Two main routes have been proposed to date to prepare such solids. The first is to directly mix two different lanthanide ions with the organic ligand before the MOF synthesis[118-121]. As an example, MIL-78 (Y, Eu) (36) or $Y_{1-x}Eu_x((C_6H_3)\text{-}(CO_2)_3)$ (with x being approximately 0.024) is a europium-doped yttrium BTB-based framework, which has been successfully synthesized under hydrothermal conditions[122]. The structure of MIL-78 (Y, Eu) was determined using PXRD data and is composed of chains of mono-capped square antiprism polyhedra and trimesate anions. The same structure was observed with rare-earth elements replacing yttrium and the doped with various rare-earth elements exhibited strong fluorescence under UV irradiation. The second possibility consists of synthesizing a first lanthanide MOF and then adding post-synthetically a second lanthanide metal ion on the defect sites of Ln-MOF and/or to replace part of the original lanthanide cations[123-125]. Dual-emitting lanthanide bimetallic MOFs may have the advantages of apparent characteristic emission, long luminescence lifetime, high emission, and bright colours visible to the naked eye when excited by UV light[126-128]. These materials often present energy transfer between the two lanthanide cations[129], making them good candidates for dual-emission ratiometric fluorescent sensing.

5.1 Bimetallic-based Ln-MOFs for sensing

Recently, Zeng et al. reported a bimetallic lanthanide MOF (ligand: H_3BTB) synthesized through a one-pot method with metal ratios (Tb/Eu) (37) of 99.5:0.5, 98:2, 95:5, and 90:10[130]. PXRD measurements showed that these structures are like those of the pure Eu- or Tb-MOFs. In addition, the emission of Eu^{3+} and Tb^{3+} could be observed in each sample under excitation at 302 nm. The authors exploited the properties of these dual Ln-MOFs for the visual sensing of a series of small organic molecules such as acetic acid, ethylenediamine, ethanol, n-butylamine, cyclohexane, and carbon tetrachloride (Fig. 9).

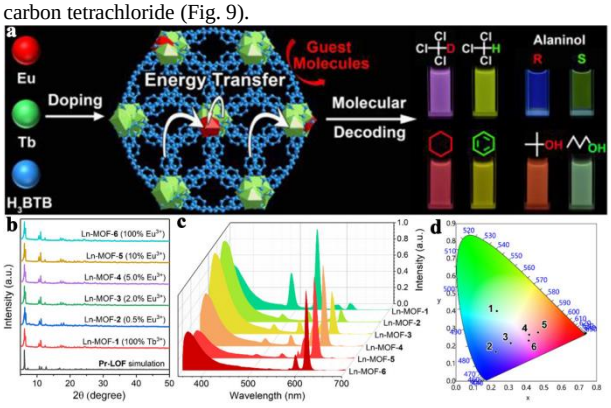

Fig. 9. (a) Schematic diagram of Ln-MOF synthesis and sensing process. Physicochemical characterization of the synthesized Ln-MOFs: (b) PXRD patterns of the different Ln-MOFs; (c) Luminescence spectra of Ln-MOFs under excitation at 302 nm; (d) CIE1931 chromaticity coordinate. [130] Copyright 2020, American Chemical Society.

The specific host-guest interactions of these small organic molecules with the dual-emission Ln-MOF are the basis for visual recognition (Fig. 10). In this study, Ln-MOF (0.5%Eu) could be used to identify n-butanol visually. N-butanol molecules were tentatively assumed to interact with the Ln open metal sites, leading to a significant red shift of BTB emission band, accompanied by enhanced red emission of MOF. However, isobutanol and tert-butanol, which are less prone to contact with metal sites due to their steric hindrance, led to a weak green luminescence, particularly for tert-butanol, the bulkiest of these two molecules. This work evidences the importance of steric hindrance to adjusting antenna effect.

5.2 Bimetallic-based Ln-MOFs nanothermometers

Photoluminescent temperature sensors have become a topic of great interest owing to numerous advantages, including simplicity, non-invasiveness, ease of operation, high resolution, ability to function in biological fluids and in the presence of strong electromagnetic fields, and rapid response[131]. Various luminescent thermometers have been proposed to date, including organic dyes, semiconductor nanocrystals, and Ln-MOFs[132-134].

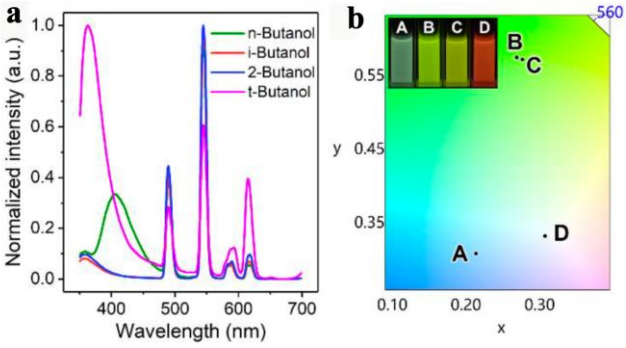

Fig. 10. (a) Photoluminescence spectra obtained from the mixture of $Eu_{0.5\%}Tb_{99.5\%}$-MOF with butanol isomer. (b) The corresponding CIE1931 chromaticity coordinates, Insets show photographs of $Eu_{0.5\%}Tb_{99.5\%}$-MOF captured under UV light irradiation. [130] Copyright 2020, American Chemical Society.

Early reported fluorescent temperature sensors were based on single emission, but the instability of the single emission band led to a lack of temperature-sensing accuracy. Therefore, developing dual-emission fluorescent temperature sensors is preferred to ensure the stability of the detection system[135, 136]. Temperature sensors shall be sensitive to a large temperature range. In addition, sensing in the near-infrared region is crucial particularly to avoid strong interference with visible light emission and for biological imaging[137-139]. Recently, Wang et al[140]. reported a near-infrared emitting bimetallic Yb-Nd-MOF(38) with characteristic emissions in the near-infrared region at 976 nm and 1057 nm under the excitation at 330 nm. The mixed-metal near-infrared dual emission MOF $Nd_{0.35}Yb_{0.65}L$ was used for near-infrared temperature sensing. In the 304-348K range, the fluorescence emission intensity of $Nd_{0.35}Yb_{0.65}L$ gradually increased as the temperature increased (Fig. 11). Still, the intensity changes of the characteristic emission band of Yb and Nd were different, and the MOF different energy transfer efficiencies between the two metal cations and ligands at different temperatures.

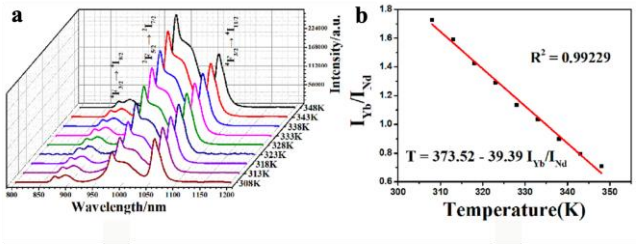

Fig. 11. (a) Temperature-dependent luminescence spectra of $Nd_{0.35}Yb_{0.65}L$. (b) the fitting curve of $Nd_{0.35}Yb_{0.65}L$ under different

temperatures. [140] Copyright 2019, Elsevier.

Table. 2 Examples of Ln-MOFs based luminescent sensors.

Name	Mechanism	Application	Excitation	Emission	Ref
$Tb_{1.7}Eu_{0.3}(BDC)_3\cdot(H_2O)_4$ (40)	Modulation of the energy transfer	Pb^{2+}	312 nm	546 nm, 616 nm	[141]
$Eu_{0.47}Tb_{0.53}$ -CTP-COOH (41)	LMCT	Fe^{3+}	280 nm	616 nm, 592 nm	[142]
$[Tb_{0.9}Eu_{0.1}(OBA)_2]\cdot(Hatz)\cdot(H_2O)_{1.5}\}_n$ (42)	Ligand-to-metal energy transfer (LMET)	Methanol	310 nm	545 nm, 618 nm	[143]
$[Me_2\text{-}NH_2][Ln(CPA)_2(H_2O)_2]$ (43)	LMCT	Iron	398 nm	617 nm	[144]
$\{[Ln_2(BIPA)_3(EG)(H_2O)_2]\}_n$ (44)	Outer-sphere interactions	Trimethylamine-N-oxide	254 nm	544 nm, 616 nm	[145]
$\{[Ln(TDA)(H_2BTEC)_{0.5}(H_2O)_3]\cdot H_2O\}_n$ (45)	Photoinduced electron transfer (PET)	5-hydroxytryptamine	280 nm	616 nm	[146]
$Tb_{97.11}Eu_{2.89}$-L1 (46)	Energy transfer	trace water in CH_3CN	280 nm	543 nm, 615 nm	[147]
$\{[Eu(L)(BPDC)_{1/2}(NO_3)]\cdot H_3O\}_n$ (47)	LMCT	Fe^{3+} ion and nitromethane	338 nm	618 nm, 545 nm	[148]
Cu/SSA/AMP-Tb (48)	LMCT	Histidine (His) and cysteine (Cys)	328 nm	549 nm	[149]
Eu-MOF Tb-MOF(49)	Coordination-induced emission	Arginine	280 nm	630 nm, 549 nm	[150]
$Eu_{0.075}Tb_{0.925}$-MOF (50)	Competively adsorbed.	Fe^{3+} or $Cr_2O_7^{2-}$	310 nm	544 nm, 614 nm	[151]
$[LnL(H_2O)_3]\cdot 3H_2O\cdot 0.75DMF$ (51)	Competition for the excitation energy	Nitrobenzene and $Cr_2O_7^{2-}$	395 nm	614 nm	[152]
Eu−QPTCA (52)	Photoinduced electron transfer	Creatine kinase ATP	373 nm	615 nm	[153]
Eu^{3+}@UiO-bpy (53)	LMCT	VOCs	380 nm	535 nm	[154]
MOF-76 (54)	Interaction among ligand and acetophenone	Monoaromatic hydrocarbons (BTEX).	296 nm	614 nm	[155]
Tb/Eu(BTC) (55)	Modulating energy transfer	Dipicolinic acid	268 nm	545 nm, 615 nm	[156]

5.3 Bimetallic-based Ln-MOFs up-conversion sensors

Upconverting MOFs are known for their ability to convert longer wavelength incident light (NIR excitation) into UV or visible light[157, 158]. They are of interest for applications such as photon/energy conversion, optical sensing, and biological imaging[159]. By coupling organic molecules with lanthanide-doped inorganic nanoparticles, the control of triplet dynamics can be achieved. This coupling mechanism, relying on spin-exchange and charge-transfer interactions, offers several advantages. Firstly, it enables the direct generation of triplet excitons from the ground state. Moreover, it facilitates efficient capture and utilization of triplet excitons, leading to improved radiative harvesting. Additionally, this coupling process introduces a novel fusion phenomenon between lanthanide and triplet excitons, resulting in highly efficient upconversion. This method may lead to Ln-MOF presenting good upconversion luminescence performances. Recent research from Zhang et al. used 1,3,5-benzene tricarboxylic acid (BTC) as an organic ligand, combined with lanthanide metals Er^{3+}, Lu^{3+}, Gd^{3+}, or Yb^{3+} and Y^{3+} to synthesize a series of bimetallic Up-MOF-$Y_{1-\chi}/Er_\chi$ (39) (range of χ is from 2% to 100%) with upconversion luminescence characteristics[87]. Up-MOF-$Y_{1-\chi}/Er_\chi$ exhibited Er upconversion characteristic emission peaks at 520, 540, and 651 nm under 980 nm excitation (Fig. 12). Besides the examples presented earlier, additional illustrations of monometallic or bimetallic Ln-MOFs used in various sensing applications are available in Table 2.

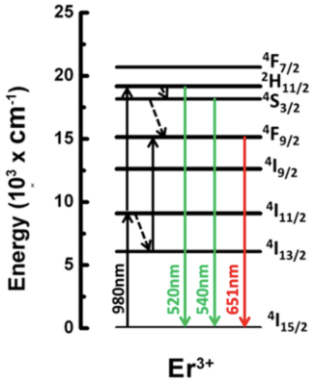

Fig. 12. Energy diagram illustrating the up-conversion process of Er^{3+} ions. [87] Copyright 2016, American Chemical Society.

6. Ln-MOFs based composites

MOFs are suitable porous materials to host guest molecules to prepare composites due to their inherently high porosity and possible defect sites [160-162]. Ln-MOF composites generally refer to the introduction of guest species (quantum dots, metal ions, dyes, noble metal nanoclusters, etc.) into Ln-MOF to construct guest molecules@Ln-MOF compounds [163-166] of interest in catalysis, imaging, sensing and other research fields [167-171]. To assess the combination mode of Ln-MOFs based composites, multiple methods could be employed. XRD can determine the stability of Ln-MOFs following the introduction of guest molecules. In addition, the N_2 sorption isotherms and TEM images of the composite can examine whether guest molecules penetrate pores or remain on the surface of Ln-MOFs.

In a fluorescence detection process, some influencing factors, such as solution concentration, temperature, type and intensity of excitation light, etc., may impact the sensitivity and discrimination ability of single-emission fluorescence sensors. To overcome these shortcomings, another chromophore might be introduced into the single-emission MOF-based luminescence sensor to construct a dual-emission ratiometric sensing platform. Its unique self-calibration ability could effectively reduce the inherent defects of single-emission sensors, thereby achieving high-sensitivity detection of target substrates[172]. For example, in Gao's work, RBH@Eu-BTC(56) composite material was synthesized by integrating post-synthesis the Rhodamine B hydrazide (RBH) dye into Eu-BTC, and the sensitization of RBH promoted the luminescence efficiency of Eu^{3+} ions[91]. The combination of RBH and Eu-MOF led to a ratiometric luminescent sensor to detect picric acid (PA) with high selectivity and sensitivity (LOD is 14 μM), where PA enhanced the emission intensity of RBH, while it quenched the characteristic emission of Eu^{3+} (Fig. 13). Transient fluorescence spectroscopy studies indicated that when PA is gradually added into the RBH@Eu-MOF system, the lifetime of the characteristic emission peak of Eu^{3+} at 616 nm gradually became shorter. On the opposite, the lifetime of RBH became longer at 555 nm, evidencing an energy transfer process from PA to RBH. The design strategy relied on PA as the fluorescence on-off switch of RBH and could inspire further development of lanthanide fluorescent sensing composite materials.

In another example, Shi and coworkers synthesized magnetic Fe_2O_3@SiO_2@Eu-MOF@Tb-MOF (MagMOF) (57) nanoballs by layer-by-layer method with core-shell structure, using terphenyl-3,4″,5-tricarboxylic acid as ligand[173].

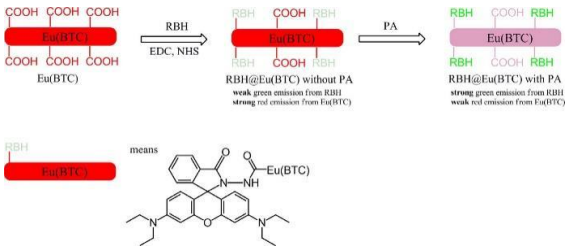

Fig. 13. Strategy to construct RBH@Eu(BTC) composites. [91] Copyright 2018, Elsevier.

The presence and stability of Eu-MOF and Tb-MOF on the surface of magnetic beads were confirmed by PXRD measurements, which remained unchanged during testing. These materials were capable of sensing biomarkers associated with acute myocardial infarction (AMI) with high sensitivity, including creatine kinase isoenzyme (CK-MB), troponin I (CTn I), and myoglobin (Mb) (Fig. 14). The limit of detection (LOD) was found to be 174.98 U/L for CK-MB, 0.16 mg L^{-1} for CTn I, and 0.94 mg L^{-1} for Mb, respectively. Additionally, the dual emission bands (Eu: 616 nm, Tb: 545 nm) of MagMOF provided a low LOD value (0.43 μM) for aspirin detection. To construct the ratiometric fluorescent sensor with a core-shell structure for biomarker detection, design strategy in this paper started with using carboxyl groups anchored on the surface of SiO_2 magnetic beads and then grew Eu-MOF and Tb-MOF on the outer layer of the magnetic beads utilizing a layer-by-layer method. This highlighted the possibility to design MOF composites of interest as multifunctional and multi-emission Ln-MOFs based detection systems using a core magnetic particle to form nanoballs that present stable luminescent signals and can form a stable suspension. The findings of this study provide a pathway for the creation of Ln-MOF-based nanoparticles using a layer-by-layer approach. One limitation of the layer-by-layer method is its lack of universal applicability to all Ln-MOFs in the synthesis of MOF magnetic nanoballs, specifically for MOFs necessitating high-temperature synthesis.

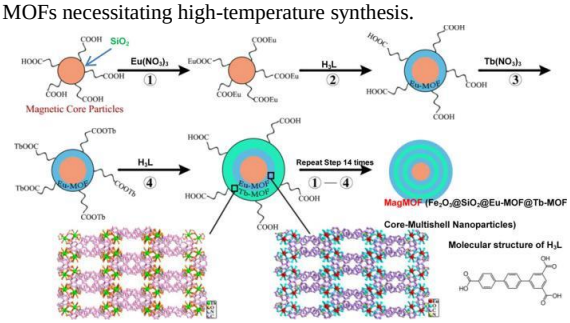

Fig. 14. Preparation scheme for hierarchically core/multi-shell Ln-MOF nanomaterials. [173] Copyright 2022, American Chemical Society.

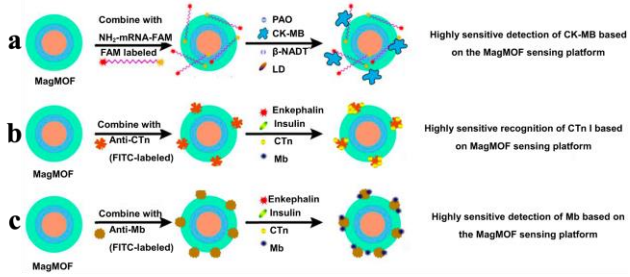

Fig. 15. MagMOF for the detection routes of AMI biomarkers: (a) CK-

MB, (b) CTn I, and (c) Mb. [173] Copyright 2022, American Chemical Society.

6.1 QDs@Ln-MOFs

Quantum dots are nanoparticles or nanocrystals with a precisely controllable size between 2-10 nm[174,175], whose composition can be adjusted to tune their electronic properties. This is of interest in spectral imaging, catalysis, sensing, and other fields[176-178]. Some quantum dots can also be small enough to enter the pores of large pores MOFs to build QDs@MOF composites[179] to improve the performance of MOFs[180]. For example, energy transfer from QDs to MOFs promotes the light-emitting properties of MOFs[181] and eventually even improves their catalytic activity[182].

Dong et al[183]. recently demonstrated the successful loading of nitrogen- and sulfur-doped carbon quantum dots into Eu-MOFs, resulting in the formation of Eu-MOFs/N, S-CDs(58) composites with strong red-light emission in organic solvents. However, the emission was significantly quenched when the composites were exposed to water (Fig. 16). Using the composites, the authors were able to detect trace amounts of water in organic solvents. However, the structure of these carbon dots remains poorly characterized, which currently limits the ability to conduct a detailed analysis of the host-guest interactions.

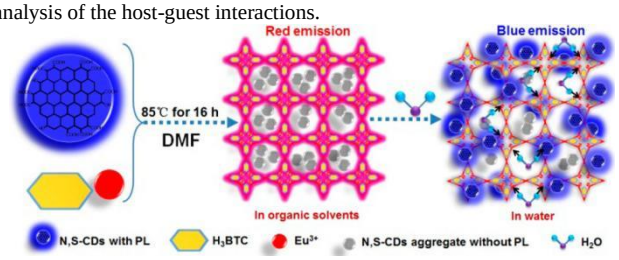

Fig. 16. Synthesis route of Eu-MOFs/N, S-CDs, and detection process of water content. [183] Copyright 2016, American Chemical Society.

Upon dispersion in DMF, the Eu-MOFs/N, S-CDs composite emitted three distinct bands located at 420, 598, and 623 nm, respectively. The peak at 420 nm originated from N, S-CDs while those at 598 nm and 623 nm originated from Eu-MOF. Gradual addition of water into the solution caused an increase in the intensity of the N, S-CDs peak, while the Eu-MOF peaks were progressively quenched (Fig. 17). In turn, the emission colour of the composite solution shifted gradually from bright red to blue with increasing water content. The self-calibrating properties of the quantum dot MOF dual-emission system provide reliable support for the detection of trace amounts of water in organic solvents.

6.2 Noble metal NPs@Ln-MOFs

Noble metal nanoparticles generally refer to metal atomic aggregation with a size between 1 and 100 nm, including gold, silver, platinum, etc[184-186], which have high electron density and dielectric properties[187]. Gold nanoparticles can be combined with various biological macromolecules and keep biological activity, widely used in immunolabeling technology[188]. Nano-silver is used in fields such as antibacterial and deodorants because of its excellent bactericidal properties[189]. Nano-platinum is a ‘star’ in catalysis, especially in energy-related research[190].

In the field of sensing, Qu et al. reported a Tb-MOF@AuNP (59) composite material as a multifunctional sensing platform to detect PSA (Prostate-Specific Antigen)[191]. The high-affinity interaction of AuNPs with PSA was the key to turn on and off the MOF luminescence (Fig. 18). In the absence of PSA, the AuNPs tended to be dispersed, and the luminescence of the Tb-MOF was quenched. With PSA, AuNPs were aggregated, and the luminescent switch of Tb-MOF was turned on. This method provides a new strategy to design turn-on detection system via the AuNPs.

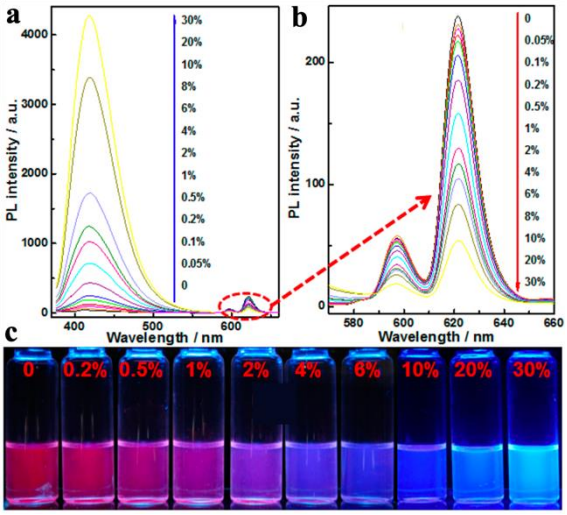

Fig. 17. (a) Photoluminescence spectra (λ_{ex} = 365 nm) of Eu-MOFs/N, S-CDs in ethanol with incremental additions of water. (b) Zoomed-in view of the red emission ion peaks in (a). (c) photographs captured under 365 nm UV light, showing Eu-MOFs/N, S-CDs added varying water contents. [183] Copyright 2016, American Chemical Society.

7. Applications

7.1 Drug sensing

Drug molecules benefit human health, but it is still hard to achieve their detection with high selectivity and high sensitivity[192, 193]. More specifically, antibiotics are a class of antibacterial and antiviral drugs widely used in humans or livestock[194], while pesticides can help crops resist pests and diseases, promote crop growth, and increase the production yield[195, 196]. However, their excessive use can damage the ecological environment[197, 198]. Therefore, it is very important to detect such harmful molecules quickly and accurately[197, 199].

Wong's research group has recently developed a highly sensitive and selective Ln-MOF sensor for detecting tetracycline antibiotics, including oxytetracycline (OTC) and tetracycline (TC), in water[200]. Out of 27 possible candidates, Tb-MOF(60) demonstrated remarkable selectivity and sensitivity towards OTC and TC. The limit of detection (LOD) for OTC and TC were determined to be 1.95 and 2.77 nM, respectively. While the mechanism underlying the sensor's selectivity and sensitivity warrants further investigation, the findings provide a promising example of Ln-MOFs being employed as effective sensors for drug molecules. For more examples of Ln-MOF used in detecting drug molecules, please refer to Table 3.

7.2 Biomarkers sensing

Biomarkers are important measurable indicators to measure the state of an organism[201]. Their concentrations are usually detected in blood, urine, or soft tissues to investigate biological processes, pathogenic processes, or pharmacological responses to realize early diagnosis. Hence, highly sensitive detection of biomarkers is essential for medical diagnosis[202-206].

Tyrosinase (TYR) is a relevant biomarker associated to some diseases[207, 208], such as melanoma, and therefore, its highly sensitive

and selective detection is extremely important for early diagnosis[209]. Recently, Yu et al. reported a quantum dot@Ln-MOF (61) composite that can be used as a dual luminescent sensor for the sensitive detection of TYR in saliva samples[210], because TYR converted L-tyrosine to boronic acid-levodopa in an alkaline borate buffer while at the same time, the red fluorescence of Eu-MOF was quenched by enhancing photo-induced electron transfer (Fig. 19).

making process (Fig. 22). Creating MOF thin films is a pathway for developing MOF-based sensors. The film can be designed to specifically target certain molecules, making it an excellent choice for developing selective sensors. Such films can also be used for other applications such as gas separation, catalysis, and energy storage[216]. Overall, creating MOF films is an important step toward the development of MOF-based sensors with high sensitivity, selectivity, and efficiency.

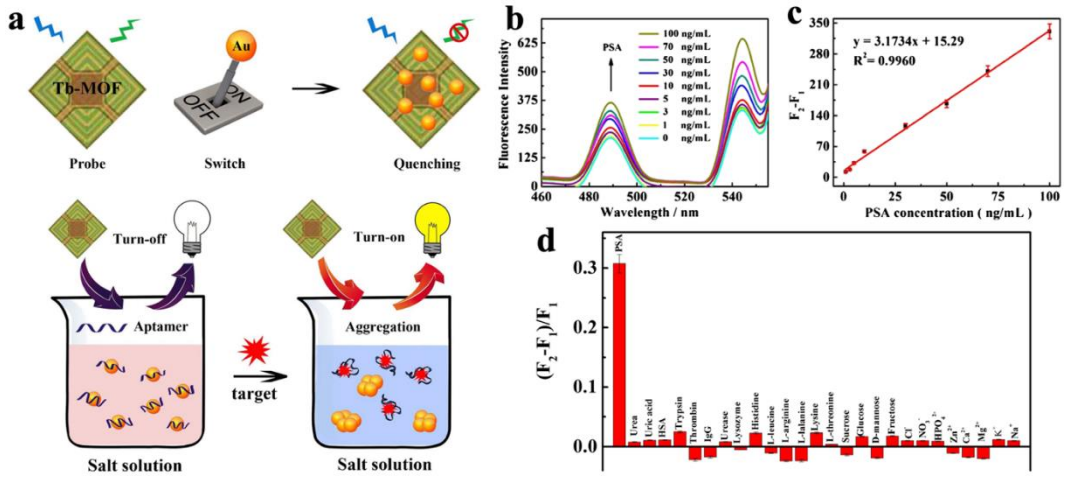

Fig. 18. (a) Schematic representation of the construction of an aptasensor utilizing the interaction between Tb-MOFs and AuNPs. (b) luminescence spectra of TB-MOF@AuNPs with addition of PSA in the NaCl solution; (c) Linear fitting relationship between PSA concentration and Tb-MOF emission difference under 545 nm. [191] Copyright 2019, Springer.

Boronic acid is a key factor in inhibiting the activity of TYR while promoting the in-situ synthesis of polymer dots. As shown in Fig. 20, in PIPES-glycine buffer, L-tyrosine is easily oxidized to melanin by TYR, as confirmed by the enhancement of the blue luminescence of the solid. This paper reported a nice strategy to detect biological enzymes using the advantages of high activity and high specificity of biological enzymes that led to the detection of target biomarkers through the action of enzyme-catalyzed products and composite materials. Other interesting examples of lanthanide MOF sensors for biomarker detection can be found in Table 4.

7.3 Temperature sensing

In different scenarios, such as in the presence of a strong electromagnetic field, intense radiation, high temperature, nanosized object, etc[211]., non-invasive temperature sensors have advantages over traditional contact temperature sensors[211-215]. Recently, Zhou et al[132]. reported an ultra-low temperature Ln-MOF based temperature-sensing thin film. First, the authors synthesized Eu-BABDC(62), Tb-BABDC(63), and by controlling the ratio of Eu and Tb, Eu_xTb_{1-x}-BABDC (x = 0.0025, 0.005, and 0.01) dual-emission lanthanide MOFs. Then, butyl methacrylate (BMA) was used as a template, and under irradiation with ultraviolet light, the mixture of Eu_xTb_{1-x}-BABDC(64) and butyl methacrylate (BMA) was copolymerized to form a single solid that was shaped into a film with certain ductility, high thermal stability, and high chemical stability (Fig. 21). The prepared Ln-BABDC-PBMA film retained the crystallinity and structure of Eu_xTb_{1-x}-BABDC. Before performing photoluminescence tests on Ln-BABDC-PBMA films, the photoluminescence properties of Ln-BABDC were investigated. The experimental results showed that $Eu_{0.0025}Tb_{0.9975}$-BABDC is an excellent photoluminescent ratiometric temperature sensor in the temperature range from 90 to 240 K. The photoluminescence tests of Tb-BABDC-PBMA, Eu-BABDC-PBMA, and $Eu_{0.0025}Tb_{0.9975}$-BABDC-PBMA films proved to be consistent with the characteristic emission of pure Ln-MOF, so Ln-MOF did not lose any luminescent properties in the film-

In another work, Yang and co-workers reported a novel method for developing a $Tb_{0.98}/Eu_{0.02}$-BTC film for temperature sensing between 298 and 383 K, by utilizing a one-step growth of mixed lanthanide MOFs on quartz substrates[217]. SEM images indicate that the thickness of the Ln-MOF film grown on the quartz substrate is approximately 420 nm, while the average size of the mixed Ln-MOF nanocrystals was observed to be within the range of 200-500 nm (Fig. 23). PXRD demonstrated that the Ln-MOF film grown on the substrate presents the same structure as that of Eu/Tb-BTC. However, the temperature sensing mechanism in play in this example should be clarified.

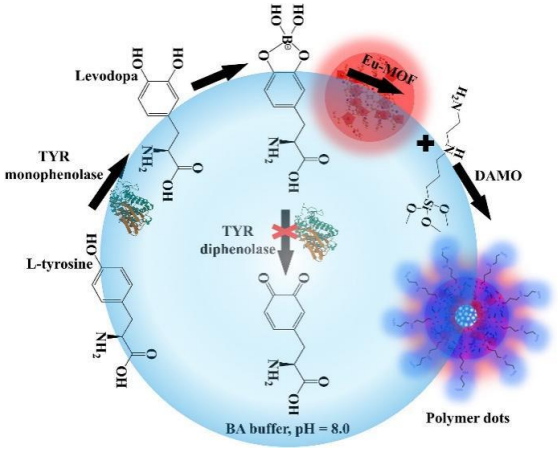

Fig. 19. Simplified pathway illustrating the dual-response turn on/off luminescence of Eu-MOF-assisted BA-levodopa polymer dots by tyrosinase mycophenolate activity. [210] Copyright 2022, Elsevier.

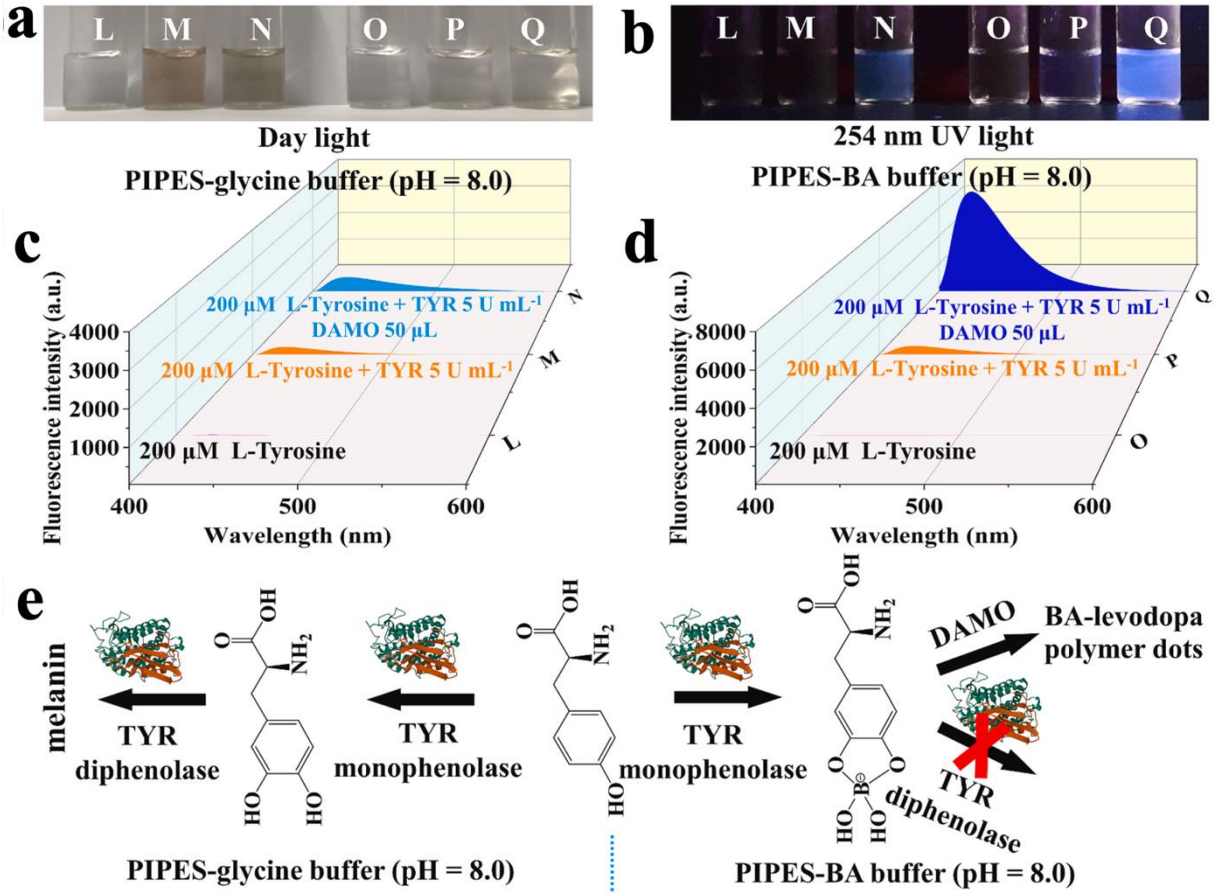

Fig. 20. Image of reaction solutions involving TYR (a) under daylight illumination, (b) under UV light at 254 nm. Solutions labelled as L, M, and N correspond to PIPES-glycine buffer (10 mM, pH 8.0), while solutions labelled as O, P, and Q correspond to PIPES-BA buffer (10 mM, pH 8.0). (c) Fluorescence emission spectra of solutions L, M, and N. (d) Fluorescence emission spectra of solutions O, P, and Q. (e) Illustration of the inhibitory effect of BA on TYR diphenolase activity. [210] Copyright 2022, Elsevier.

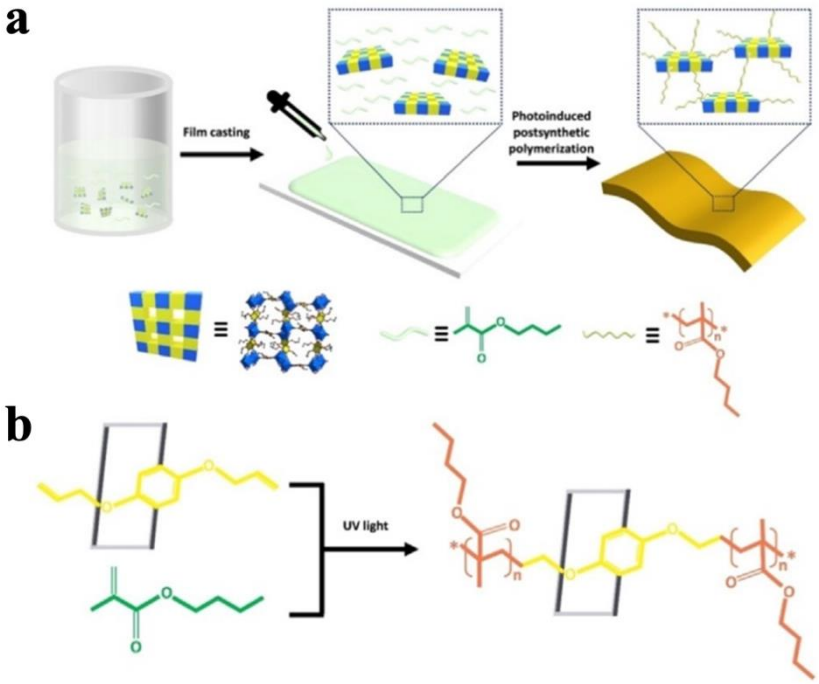

Fig. 21. Formation route of a polyMOF hybrid membrane via the copolymerization of Ln-BABDC with butyl methacrylate monomers. [132] Copyright 2020, Wiley-VCH Verlag.

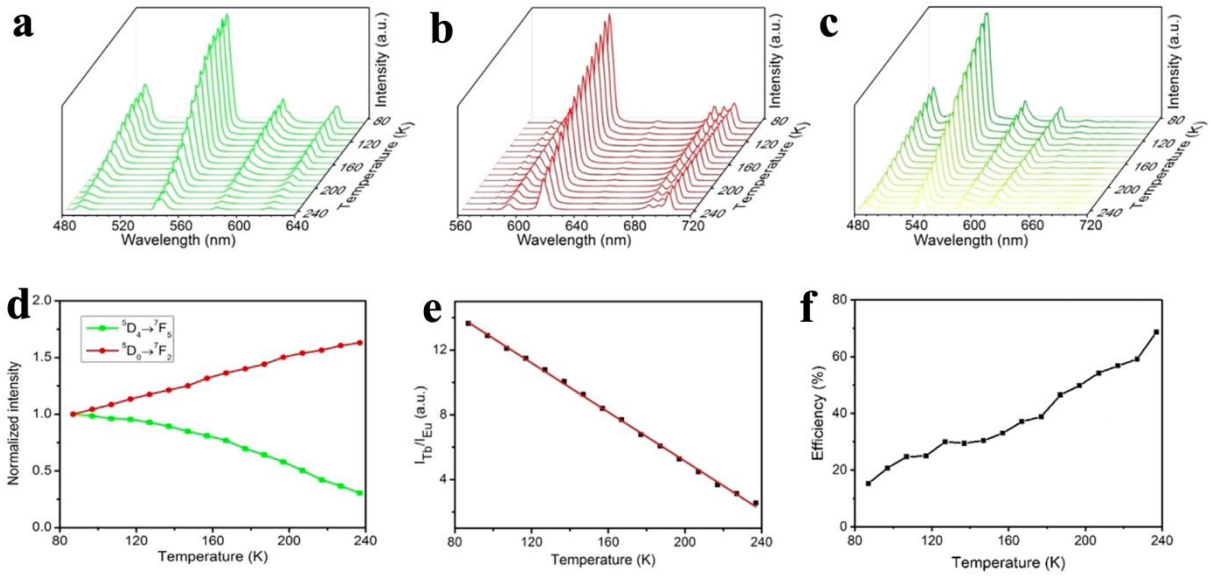

Fig. 22. Under different temperature (a) Emission spectra of Tb-BABDC-PBMA membrane, (b) Eu-BABDC-PBMA membrane, (c) $Eu_{0.0025}Tb_{0.9975}$-BABDC-PBMA membrane. (d) Temperature dependence of the integrated intensities of the $^5D_4 \rightarrow {}^7F_5$ (545 nm) and $^5D_0 \rightarrow {}^7F_2$ (617 nm) transitions for the $Eu_{0.0025}Tb_{0.9975}$-BABDC-PBMA membrane. (e) Fitted curves of the integrated intensity ratio for the $Eu_{0.0025}Tb_{0.9975}$-BABDC-PBMA membrane in the temperature range of 90-240 K. (f) Energy transfer efficiency for the $Eu_{0.0025}Tb_{0.9975}$-BABDC-PBMA membrane between Tb^{3+} and Eu^{3+} ions at various temperatures. [132] Copyright 2020, Wiley-VCH Verlag.

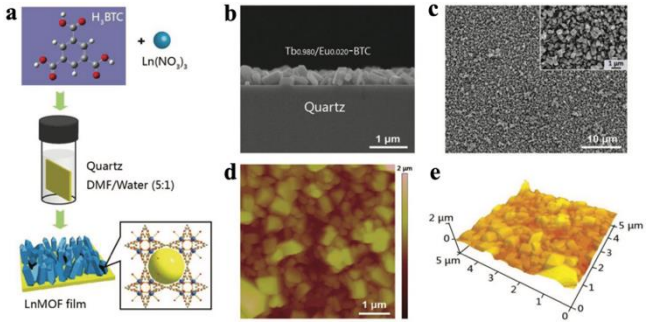

Fig. 23. (a) Schematic diagram illustrating the preparation process of mixed Ln-MOF thin films. (b, c) Cross-sectional and top-view scanning electron microscopy (SEM) images of the $Tb_{0.98}/Eu_{0.02}$-BTC films. (d, e) Atomic force microscopy (AFM) image and the corresponding 3D representation of the $Tb_{0.98}/Eu_{0.02}$-BTC film. [217] Copyright 2019, Wiley-VCH Verlag.

The temperature sensing ability of $Tb_{0.98}/Eu_{0.02}$-BTC(65) film was evaluated over a temperature range of 298-383 K with excitation at 260 nm. The emission peak intensity of Eu^{3+} at 617 nm displayed a gradual increase with temperature, whereas the emission peak intensity of Tb^{3+} at 549 nm decreased due to energy transfer from Tb^{3+} to Eu^{3+} (as observed in Fig. 24). These findings highlight the potential of Ln-MOF based luminescent sensing thermometers as non-contact temperature measurement tools, with numerous applications in high-tech fields. Compared to other fluorescent materials (e.g. quantum dots or organic dyes), Ln-MOFs offer sharper and narrower emission bands, higher temperature sensitivity due to the energy difference between excitation and emission wavelengths, and thus are an excellent choice for temperature sensing. Examples of other Ln-MOF temperature sensors can be seen in Table 5.

7.4 Ln-MOFs-based luminescent arrays

Luminescence sensing is widely used in the field of molecular recognition due to its high sensitivity[218], ultra-low detection limit, simple operation, and low cost[219-223]. However, when used to detect real samples, the complex detection environment affects the sensitivity and selectivity of fluorescence sensing[224, 225]. Identifying and quantifying specific substances can be accomplished by leveraging the characteristic maps generated by each sensing unit in a luminescent sensing array, composed of a series of interconnected units[226, 227]. Sensing arrays have outstanding advantages, especially for the analysis of mixed samples,[228] and have therefore been widely used in many practical detection environments.

Luminescent sensing arrays of pure lanthanide MOFs are commonly constructed from bimetallic Ln-MOFs. The dual-emission characteristics of these materials allow for the utilization of specific emission sites as sensing units in luminescent sensing arrays. For instance, Xie et al[229]. have recently developed a ratiometric luminescent sensor array based on Eu/Tb-MOFs(66) that can interact with multiple antibiotics (as shown in Fig. 25). The response of the sensor array is measured as the luminescence intensity ratio at 545 nm to 616 nm (F_{545}/F_{616}), which exhibits different values for different antibiotics. Eight antibiotics could be distinguished from 25 antibiotics by principal component analysis (PCA). More examples can be found in Table 6.

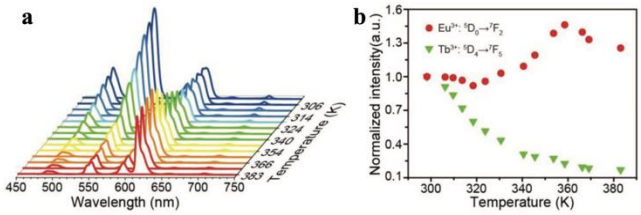

Fig. 24. (a) Luminescent spectra of the $Tb_{0.98}/Eu_{0.02}$-BTC film from 298 K to 383 K under excitation at 296 nm. (b) The normalized emission intensity of Tb^{3+} ($^5D_4 \rightarrow {}^7F_5$) and Eu^{3+} ($^5D_0 \rightarrow {}^7F_2$) transitions at different temperature. [217] Copyright 2019, Wiley-VCH Verlag.

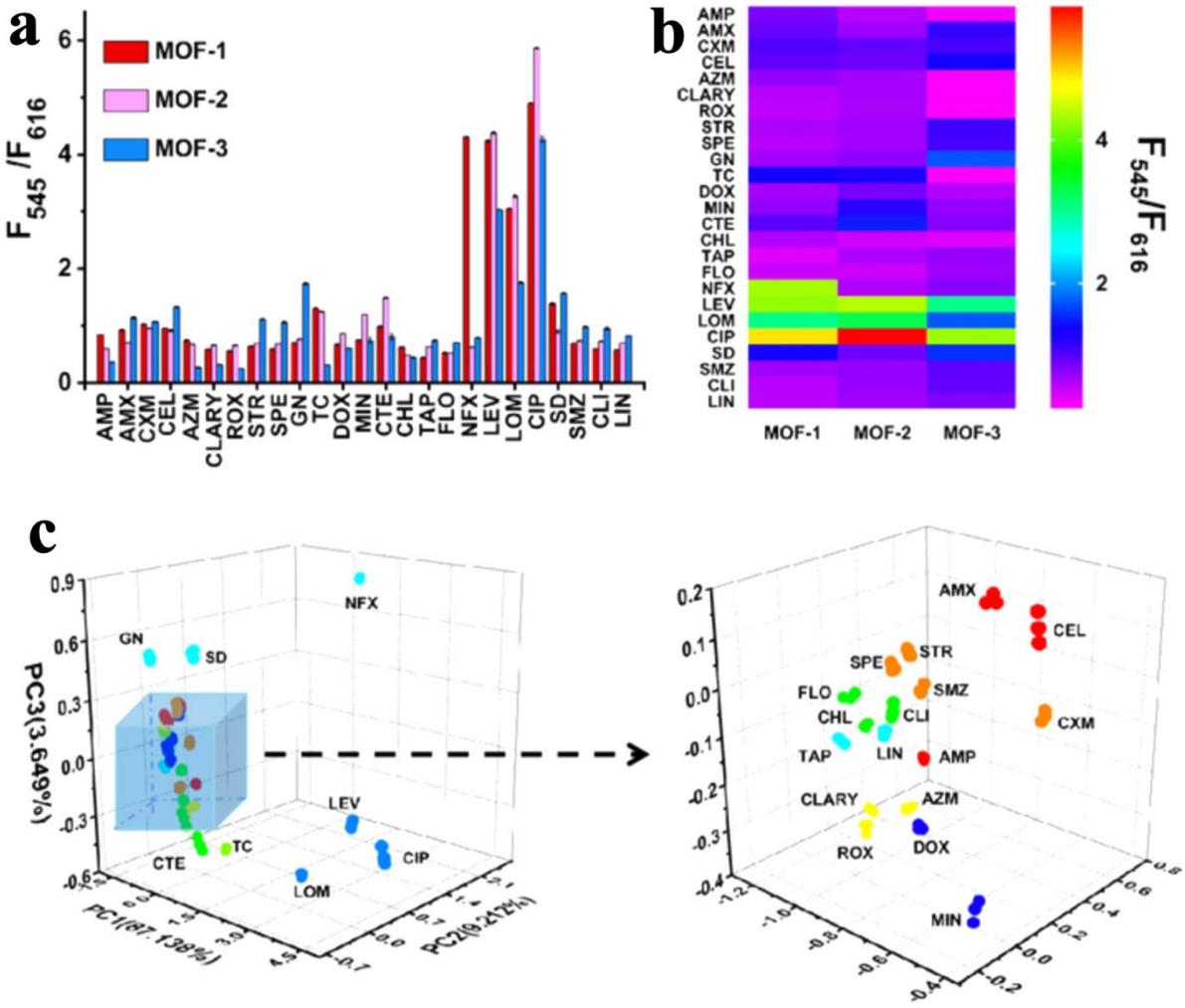

Fig. 25. (a) Luminescence ratio changes (F_{545}/F_{616}) of 25 antibiotics after 30 minutes (1 mM). (b) Heatmap representing the response patterns of the sensor array to the same set of antibiotics (1 mM). (c) Canonical score plot obtained from PCA analysis depicting luminescence responses against the 25 antibiotics (1 mM). [229] Copyright 2021, Elsevier.

7.5 Other applications

In addition to the aforementioned applications, Ln-MOFs are being explored in various other fields such as pH sensing, VOC (Volatile Organic Compounds) detection, anion and cation sensing, etc. For instance, Li et al[230]. have reported on the use of a viologen-functionalized m-benzene dicarboxylate organic linker for the preparation of a new tetranuclear 3D Tb oxo cluster-based MOF with potential for pH luminescent sensing. The organic ligands in this MOF offer unique active sites with varying protonation levels, which makes it suitable as a pH luminescent sensor. Interestingly, the luminescence intensity of the MOF exhibited a good linear relationship with pH over the range of 2-7 (Fig. 26). Some typical examples are listed in Table 7 for reference. Exploring and developing other application fields of Ln-MOFs is still a direction under continuous development.

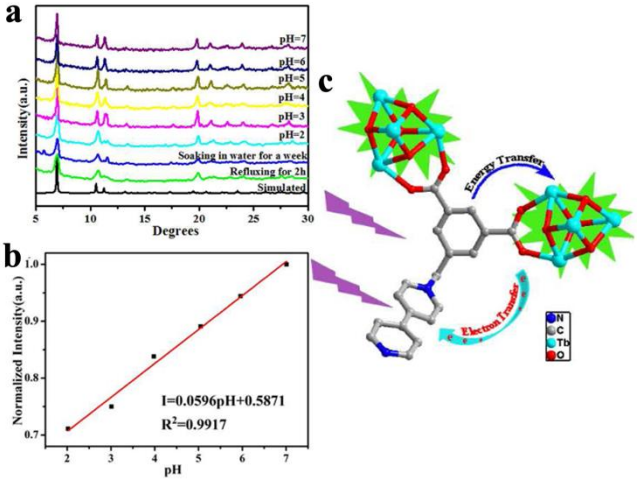

Fig 26. (a) Powder X-ray diffraction patterns of Tb-MOF(67) samples immersed in boiling water and under different pH values of 2, 3, 4, 5, 6, and 7 water solution. (b) Linear correlation between emission intensity of Tb-MOF (542 nm) after adding different pH values aqueous solutions (c) scheme of energy transfer and electron transfer mechanisms in Tb-MOF. [230] Copyright 2015, American Chemical Society.

Table 3. Examples of Ln-MOFs based drug sensing

Name	Analyte	Excitation	Emission	Ref
[Tb(HL)L(H_2O)]n (68)	Tetracycline antibiotics	361nm	542nm	[231]
MLMOF-3 (69)	Coumarin	285nm	547nm, 619nm	[232]
Eu^{3+}@Gd-MOF (70)	Ciprofloxacin	315nm	371nm, 614nm	[233]
$Eu_2[Ru(dcbpy)_3]_3$ (71)	Trenbolone	300 nm	635nm	[234]
$Ce_{0.2}Tb_{0.8}$-tbia (72)	captopril	330nm	545nm	[235]

Table 4. Examples of Ln-MOFs-based biomarker sensing.

Name	Analyte	Excitation	Emission	Ref
B-EuMOF (73)	N-acetylneuraminic acid	356 nm	470 nm, 614 nm	[84]
Tb-PTA-OH (74)	DPA	275 nm	436 nm, 551nm	[100]
Ln-MOF (75)	HIAA	280 nm	616 nm	[146]
Eu-QPTCA (76)	Creatine kinase	373 nm	615 nm	[153]
Ga(OH)(btec) • $0.5H_2O$ (77)	1-Hydroxypyrene	302 nm	614 nm	[236]

Table 5. Examples of Ln-MOFs based temperature sensing

Name	Temperature range	Excitation	Emission	Ref
Eu^{3+}@UiO-bpydc (78)	293-353K	340 nm	530 nm, 614 nm	[80]
Ln-BABDC-PBMA (79)	90-240K	370 nm	545 nm, 617 nm	[132]
$Tb_{0.98}/Eu_{0.02}$-BTC film (80)	298-383K	296 nm	549 nm, 617 nm	[217]
EuW_{10}@Tb-TATB (81)	200-320K	330 nm	541 nm, 617 nm	[237]
UiO-66(Zr&Eu)-1 film (82)	237-337K	360 nm	420 nm, 617 nm	[238]

Table 6. Examples of Ln-MOFs based luminescent arrays.

Name	Mechanism	Application	Excitation	Emission	Ref
MOF-253⊃Eu^{3+} (83)	Energy transfer	Metal ions	350 nm	420 nm, 520 nm, 617 nm	[75]
Eu-MOFs/N,S-CDs (84)	Energy transfer	Water in Organic Solvents	365 nm	420 nm, 623 nm	[183]
Tb-MOFs@AuNPs (85)	IFE dynamic quenching effect (DQE) FRET	Prostate-specific antigen (PSA)	280 nm	545 nm	[191]
Eu/Tb@Zn-MOF (86)	“Lock-key” mechanism	Antibiotics	330 nm	616 nm, 545 nm	[229]
MoS_2 QDs-Eu-MOF (87)		Tetracycline	400 nm	620 nm, 470 nm	[239]
CDs@Eu-MOFs (88)	Resonance energy transfer (RET) Inner Filter effect (IFE)	Chromium Cr(VI)	390 nm	467 nm, 616 nm	[240]
BYCDs@ZIF-8 (89)	Static quenching	glutathione	365 nm	440 nm, 565 nm	[241]
CTGU-1 (90)	Ligand-to-metal energy transfer	Eu^{3+} and Dy^{3+}		589 nm	[242]
Tb-MOF@PDDA-aggregated-AuNP (91)	FRET	Chlorpyrifos	290 nm	544 nm	[243]
Tb-MOFs@SH-AuNP (92)	Synergistic effect of IFE, DQE and FRET	Adenosine triphosphate (ATP)	290 nm	547 nm	[244]
La(III)-MOF/Ag NPs (93)	FRET	MiRNA-155		450 nm	[245]
Zn-TbMOF Zn-EuMOF (94)	Energy transfer	Phosphates	280 nm	616 nm, 545 nm	[246]
$Tb_{1-x}Eu_x$-CTP-COOH (95)	FRET, Photo-induced electron transfer (PET), IFE	Natural medicine	260 nm	615 nm, 595 nm 545 nm, 490 nm	[247]
LMOFs (96)	Dynamic quenching mechanism	Anionic Sulfonate Surfactants	330 nm		[248]
Ln-MOF 1–3 (97)	Energy transfer	Multiple antibiotics	320 nm	430 nm, 490 nm, 548 nm, 618 nm	[249]
Eu@UiO-66-$(COOH)_2$ and Tb@UiO-66-$(COOH)_2$ (98)	Host-guest recognition effect	Baijiu	320 nm	615 nm, 542 nm	[250]
EuTb(HFA)n@ZY (99)	Energy transfer	Amines	302 nm	544nm, 612 nm	[251]

Table 7. Ln-MOFs for other applications.

Name	Application	Excitation	Emission	Ref
$Eu_{0.07}Gd_{0.03}$-MOF (100)	Fe^{3+}, Vitamin C	315 nm	415 nm, 614 nm	[82]
Eu-DPA (101)	Tyrosinase	275 nm	423 nm, 622 nm,	[210]
Eu-MOF/Nafion hybrid (102)	pH sensing: 2-7	336 nm	542 nm	[230]
Tb-MOF (103)	pH sensing: 6-12.5	415 nm	650 nm	[252]
YTMNs (104)	pH sensing: 0.2-11	235 nm	545 nm	[253]
DMF-Tb-PhenMOF nanoparticles (105)	pH sensing: 1-11	335 nm	615 nm	[254]
Eu^{3+}@UiO-67-bpydc (106)	pH sensing: 3-10	330 nm	616 nm	[255]
Tb/Eu (TATB) (107)	F^-	320 nm	545 nm, 617 nm	[256]
$Eu_{0.67}Tb_{0.33}$-CP (108)	CrO_4^{2-}	325 nm	386 nm, 545 nm, 616 nm	[257]
Eu-k-bpda (109)	Heavy atom and cysteine	343 nm	615 nm	[258]

8. Conclusions and outlooks

Recognition targets often include chemical molecules (anions, gases, etc.), biological macromolecules (proteins, enzymes, DNA, etc.), temperature, etc. Currently, there are many materials available for luminescent sensing. However, MOFs are unique, especially Ln-MOFs, as their structural and chemical versatility endows them with enormous potential to introduce post-synthetically specific functional groups combined with the intrinsic porosity to design multifunctional detection platforms. At the same time, Ln-MOFs composites with tunable luminescence have also received continuous attention. Furthermore, the atomic-level structural periodicity of MOFs allows for a better understanding of underlying detection mechanisms compared to other materials.

Considering the above-mentioned advantages of MOFs, many exciting examples of MOF based sensors have been reported recently. However, some issues still require special attention when considering Ln-MOF-based luminescent sensors in realistic detection environments. First, the stability of MOFs has different requirements in different detection environments, so the chemical and thermal stability of MOFs shall be continuously studied in real conditions. For sensing small molecules, cations, anions, etc., the interaction between detection substrates and MOFs may destroy or contaminate the MOF framework, which could be checked by PXRD, IR, TGA, among other techniques. Second, for bioluminescent sensing, the water stability of MOFs is a prerequisite, and one shall consider N_2 porosimetry and electron microscopy to confirm their water stability in addition to PXRD analysis.

A comparison of the optical properties of Ln-MOFs with other luminescent materials used for sensing evidences the potential advantage of intrinsic porosity of MOFs, which can be of strong interest to target/concentrate analyst molecules, to strengthen host-guest interactions and further improve their detection sensitivity. The large energy difference between the excitation and emission wavelengths combined with the sharp and narrow emission bands in Ln-MOFs might also enhance the sensitivity for easier observation of the variation of the luminescent signal during detection progress.

With the continuous development of Ln-MOFs based composites, their photoluminescence and sensing mechanisms are gradually being better understood. We are convinced that further developing MOF based light-emitting composites with excellent performance and stability suitable for practical detection environments is a promising direction to construct better performance sensing devices such as holographic sensors, fiber optic sensors, contact lens sensors, dermal sensors, or wearable sensors.

Abbreviations

Ln-MOFs	Lanthanide metal-organic frameworks
LMCT	Ligand-to-metal energy transfer
LLET	Ligand-ligand energy transfer
MLCT	Metal-to-ligand charge transfer
ICT	Intramolecular charge transfer
NPs	Nanoparticles
SBUs	Secondary Building Units
LOD	Limit of detection
QD	Quantum yield
BEnT	Back energy transfer
ESA	Excited state absorption
IFE	Inner filter effect
VOC	volatile organic compound
PXRD	Powder X-Ray Diffraction
TEM	Transmission Electron Microscopy
SEM	Scanning Electron Microscopy
BET	Brunauer-Emett-Teller
TGA	Thermogravimetric analysis
UV-vis	Ultraviolet visible
SCXRD	Single-crystal X-ray diffraction
BA-Eu-MOF	Boronic acid (BA) functionalized Eu-MOF
MMCF-4	L=5,5′,5″-((1,4,7triazonane1,4,7-riyl)
$[Tb(L)]\cdot(H_2O)n$	tris(methylene))triisophthalic acid
MIL-78(Y,Eu)	$Y_{1-x}Eu_x((C_6H_3)\text{-}(CO_2)_3)$
MagMOF	Fe_2O_3@SiO_2@Eu-MOF@Tb-MOF
TYR	Tyrosinase
PCA	Principal component analysis
PSA	Prostate-Specific Antigen
OTC	Oxytetracycline
TC	Tetracycline
QDs	Quantum dots
PA	picric acid
RBH	Rhodamine B
CK-MB	Creatine kinase isoenzyme
AMI	Acute myocardial infarction
$Nd_{0.35}Yb_{0.65}L$	L = terphenyl-3,4″,5-tricarboxylic acid
BABDC	5-bis(allyloxy)terephthalic acid
H_3BTB	3,5 Benzene tris-benzoate
H_4BTEC	2,4,5-benzenetetracarboxylic acid
H_3BTC	Benzene-1,3,5-tricarboxylate
H_2NDC	2,6-naphthalene dicarboxylic acid

H_2bpy	2,2'-bipyridine-5,5'-dicarboxylic acid
H_4QPTCA	1,1':4',1'':4'',1'''-quaterphenyl-3,3''',5,5'''-tetracarboxylic acid
H_2tfBDC	2,3,5,6-tetrafluoroterephthalic acid
H_2BDC	Benzene-1,4- dicarboxylate
H_2OBA	4,4′-oxybis(benzoate) acid,
Hatz	3-amino-1,2,4-triazole
H_2CPA	5-(4-carboxy phenyl)picolinic acid
H_2BIPA	5-boronoisophthalic acid
H_4BTEC	1,2,4,5-benzenetetracarboxylic acid
H_2TDA	Thiazolidine 2,4-dicaboxylic acid
H_3L_2	4,4′,4″-(pyridine-2,4,6-triyl)tris(benzoic acid)
H_3tcptp	4-(2,4,6-tricarboxyl phenyl)-4,2′:6′,4″-terpyridine
H_4btca	benzene-1,2,3,5-tetracarboxylic acid
H_2atpt	Aminoterephthalic acid
H_2BPTA	2,5-bis(pyrazol-1-yl) terephthalic acid
PTA	P-phthalic acid
PTC	Pyromellitic acid
BPTC	biphenyl-3,3,5,5-tetracarboxylic acid
BPDC	Biphenyl-4,4'-dicarboxylic acid
H_3TATB	Triazine-1,3,5-tribenzoic acid
H_2FDA	Furan-2,5-dicarboxylic acid
H_2bpda	2,2′-bipyridine-6,6′-dicarboxylic acid

Author Contributions

Xinrui Wang wrote the original manuscript, Yupeng Jiang collected and organized all the references and tables. Christian Serre and Antoine Tissot corrected the manuscript.

Declaration of competing interest

All the authors have not any conflicts of interest.

Acknowledgements

Xinrui Wang appreciates the support from CSC grant (grant number: 201908120131). Xinrui Wang also thanks Prof. S. Petoud, Prof. B. Ding and Dr. S. Perruchas's precious suggestions for manuscript correction.

REFERENCES

[1] Z.Q. Zhao, S. Yang, M.C. Zhu, Y. Zhang, Y.G. Sun, S.Y. Wu, Sensors and Actuators B-Chemical, 383 (2023).
[2] Y.N. Zhou, S.J. Zhao, W.X. Leng, X. Zhang, D.Y. Liu, J.H. Zhang, Z.G. Sun, Y.Y. Zhu, H.W. Zheng, C.Q. Jiao, Inorganic Chemistry, (2023).
[3] X.T. Zhang, H.Y. Qiu, W. Luo, K.F. Huang, Y. Chen, J.C. Zhang, B.H. Wang, D.L. Peng, Y. Wang, K.Z. Zheng, Advanced Science, 10 (2023).
[4] X.L. Yu, A.A. Ryadun, D.I. Pavlov, T.Y. Guselnikova, A.S. Potapov, V.P. Fedin, Angewandte Chemie-International Edition, (2023).
[5] S. Wang, T. Pirzada, W. Xie, E. Barbieri, O. Hossain, C.H. Opperman, L. Pal, Q. Wei, G.N. Parsons, S.A. Khan, Applied Materials Today, 28 (2022) 101517.
[6] Y.-Z. Li, G.-D. Wang, W.-J. Shi, L. Hou, Y.-Y. Wang, Z. Zhu, ACS Applied Materials & Interfaces, 12 (2020) 41785-41793.
[7] X.L. Zhuang, S.T. Zhang, Y.J. Tang, F. Yu, Z.M. Li, H. Pang, Coordination Chemistry Reviews, 490 (2023).
[8] W.X. Zhou, Y.J. Tang, X.Y. Zhang, S.T. Zhang, H.G. Xue, H. Pang, Coordination Chemistry Reviews, 477 (2023).
[9] N. Zhang, J.C. Wang, Y.F. Guo, P.F. Wang, Y.R. Zhu, T.F. Yi, Coordination Chemistry Reviews, 479 (2023).
[10] Z.J. Zhu, R. Tang, C.R. Li, X.D. An, L. He, Advanced Science, (2023).
[11] P.Y. Zhou, J.J. Lv, X.B. Huang, Y.F. Lu, G. Wang, Coordination Chemistry Reviews, 478 (2023).
[12] K. Yonesato, D. Yanai, S. Yamazoe, D. Yokogawa, T. Kikuchi, K. Yamaguchi, K. Suzuki, Nature Chemistry, 15 (2023) 940-+.
[13] T. Simon-Yarza, A. Mielcarek, P. Couvreur, C. Serre, Advanced Materials, 30 (2018).
[14] T. Simon-Yarza, M. Gimenez-Marques, R. Mrimi, A. Mielcarek, R. Gref, P. Horcajada, C. Serre, P. Couvreur, Angewandte Chemie-International Edition, 56 (2017) 15565-15569.
[15] A.C. McKinlay, R.E. Morris, P. Horcajada, G. Ferey, R. Gref, P. Couvreur, C. Serre, Angewandte Chemie-International Edition, 49 (2010) 6260-6266.
[16] X.Z. Wang, Z.Q. Zhang, R. Guo, Y.Y. Zhang, N.J. Zhu, K. Wang, P.P. Sun, X.Y. Mao, J.J. Liu, J.Z. Huo, X.R. Wang, B. Ding, Talanta, 217 (2020).
[17] X.Z. Wang, X.Y. Mao, Z.Q. Zhang, R. Guo, Y.Y. Zhang, N.J. Zhu, K. Wang, P.P. Sun, J.Z. Huo, X.R. Wang, B. Ding, Inorganic Chemistry, 59 (2020) 2910-2922.
[18] X.Z. Wang, J. Du, N.N. Xiao, Y. Zhang, L. Fei, J.D. LaCoste, Z. Huang, Q. Wang, X.R. Wang, B. Ding, Analyst, 145 (2020) 4646-4663.
[19] X.Z. Wang, X.R. Wang, Y.Y. Liu, J.Z. Huo, Y. Li, Q. Wang, K. Liu, B. Ding, Ultrasonics Sonochemistry, 59 (2019).
[20] X.R. Wang, X.Z. Wang, J. Du, Z. Huang, Y.Y. Liu, J.Z. Huo, K. Liu, B. Ding, Journal of Solid State Chemistry, 279 (2019).
[21] J.Y. Zhu, B.S. He, L.L. Xie, X.Y. Cao, Y. Liang, J.S. Wang, Sensors and Actuators B-Chemical, 382 (2023).
[22] Z. Liu, X.X. Wang, R. Guo, J.J. Richardson, T.Z. Wang, W.J. Xu, F. Caruso, S.J. Pan, Advanced Functional Materials, (2023).
[23] H. Qutaish, J.H. Suh, S.A. Han, S. Kim, M.S. Park, J.H. Kim, Applied Surface Science, 605 (2022).
[24] Z.L. Zheng, H.L. Nguyen, N. Hanikel, K.K.Y. Li, Z.H. Zhou, T.Q. Ma, O.M. Yaghi, Nat Protoc, 18 (2023) 136-156.
[25] J.-L. Wang, X.-Y. Hu, C.-G. Han, S.-Y. Hou, H.-S. Wang, F. Zheng, Acs Nano, 16 (2022) 14827-14837.
[26] Y.-B. Hao, Z.-S. Shao, C. Cheng, X.-Y. Xie, J. Zhang, W.-J. Song, H.-S. Wang, ACS Applied Materials & Interfaces, 11 (2019) 31755-31762.
[27] H.-S. Wang, H.-L. Liu, K. Wang, Y. Ding, J.-J. Xu, X.-H. Xia, H.-Y. Chen, Analytical Chemistry, 89 (2017) 11366-11371.
[28] H.-S. Wang, J. Li, J.-Y. Li, K. Wang, Y. Ding, X.-H. Xia, Npg Asia Mater, 9 (2017) e354-e354.
[29] Y. Xie, G.T. Sun, J.W. Li, L.N. Sun, Advanced Functional Materials, (2023).
[30] X.R. Wang, X.Z. Wang, Y. Li, K. Liu, S.X. Liu, J. Du, Z. Huang, Y. Luo, J.Z. Huo, X.X. Wu, Y.Y. Liu, B. Ding, Ultrasonics Sonochemistry, 44 (2018) 340-349.
[31] X.R. Wang, X.Z. Wang, Y. Li, J. Du, S.X. Liu, Y. Luo, J.Z. Huo, Y.Y. Liu, X.X. Wu, B. Ding, Zeitschrift Fur Anorganische Und Allgemeine Chemie, 644 (2018) 357-366.
[32] X.R. Wang, Z. Huang, J. Du, X.Z. Wang, N. Gu, X. Tian, Y. Li, Y.Y. Liu, J.Z. Huo, B. Ding, Inorganic Chemistry, 57 (2018) 12885-12899.
[33] X.R. Wang, J. Du, Z. Huang, K. Liu, Y.Y. Liu, J.Z. Huo, Z.Y. Liu, X.Y. Dong, L.L. Chen, B. Ding, Journal of Materials Chemistry B, 6 (2018) 4569-4574.
[34] Y.Y. Zhang, J. Mao, P.F. Zhu, G.F. Wang, Nano Research, (2023).
[35] Y.J. Yang, Y. Liu, D.T. Tu, M.M. Chen, Y.Q. Zhang, H. Gao, X.Y. Chen, Angewandte Chemie-International Edition, 61 (2022).
[36] P. Huo, Z. Li, R. Yao, Y. Deng, C. Gong, D. Zhang, C. Fan, S. Pu, Spectrochimica Acta Part A: Molecular and Biomolecular Spectroscopy, 282 (2022) 121700.
[37] S. SeethaLekshmi, A.R. Ramya, M.L.P. Reddy, S. Varughese, Journal of Photochemistry and Photobiology C: Photochemistry Reviews, 33 (2017) 109-131.
[38] D. Zhang, Y. Zhou, J. Cuan, N. Gan, CrystEngComm, 20 (2018) 1264-1270.
[39] J. Tang, X. Huang, Y. Wang, J. Liu, Optical Materials, 29 (2007) 1774-1781.
[40] M. Kawa, J.M.J. Fréchet, Chemistry of Materials, 10 (1998) 286-296.
[41] Q. Du, P. Wu, P. Dramou, R. Chen, H. He, New Journal of Chemistry, 43 (2019) 1291-1298.

[42] L. Xiong, L. Yu, S. Li, L. Feng, Y. Xiao, Microchim Acta, 188 (2021) 236.
[43] R. Sakamoto, N. Fukui, H. Maeda, R. Toyoda, S. Takaishi, T. Tanabe, J. Komeda, P. Amo-Ochoa, F. Zamora, H. Nishihara, Coordination Chemistry Reviews, 472 (2022) 214787.
[44] R. Zhang, L. Zhu, B. Yue, Chinese Chem Lett, 34 (2023) 108009.
[45] C. Serre, G. Férey, Journal of Materials Chemistry, 12 (2002) 3053-3057.
[46] C. Serre, N. Stock, T. Bein, G. Férey, Inorganic Chemistry, 43 (2004) 3159-3163.
[47] F. Millange, C. Serre, J. Marrot, N. Gardant, F. Pellé, G. Férey, Journal of Materials Chemistry, 14 (2004) 642-645.
[48] C. Serre, F. Pelle, N. Gardant, G. Ferey, Chemistry of Materials, 16 (2004) 1177-1182.
[49] C. Serre, J. Marrot, G. Férey, Inorganic Chemistry, 44 (2005) 654-657.
[50] S. Surblé, C. Serre, F. Millange, F. Pelle, G. Férey, Solid State Sci, 7 (2005) 1074-1082.
[51] S. Surblé, C. Serre, F. Millange, G. Férey, Solid State Sci, 8 (2006) 413-417.
[52] N. Stock, S. Biswas, Chemical Reviews, 112 (2012) 933-969.
[53] F. Pellé, S. Surblé, C. Serre, F. Millange, G. Férey, Journal of Luminescence, 122-123 (2007) 492-495.
[54] M. Bosch, S. Yuan, W. Rutledge, H.-C. Zhou, Accounts of Chemical Research, 50 (2017) 857-865.
[55] C. Serre, F. Millange, S. Surblé, G. Férey, Angew Chem Int Ed Engl, 43 (2004) 6285-6289.
[56] T. Devic, C. Serre, N. Audebrand, J. Marrot, G. Férey, Journal of the American Chemical Society, 127 (2005) 12788-12789.
[57] H. Pu, Y. Xie, Q. Wei, D.-W. Sun, Microchem J, 190 (2023) 108563.
[58] T. Wiwasuku, A. Chuaephon, U. Habarakada, J. Boonmak, T. Puangmali, F. Kielar, D.J. Harding, S. Youngme, ACS Sustainable Chemistry & Engineering, 10 (2022) 2761-2771.
[59] P. Yang, J. Wang, S. Wang, C. Yang, P. Zhao, B. Huang, Q. Wang, H. Wang, Acs Omega, 7 (2022) 37452-37464.
[60] P.P. Bag, X.-S. Wang, R. Cao, Dalton Transactions, 44 (2015) 11954-11962.
[61] M. Almáši, V. Zeleňák, J. Kuchár, S. Bourrelly, P.L. Llewellyn, Colloids and Surfaces A: Physicochemical and Engineering Aspects, 496 (2016) 114-124.
[62] H.N. Abdelhamid, M. Wilk-Kozubek, A.M. El-Zohry, A. Bermejo Gómez, A. Valiente, B. Martín-Matute, A.-V. Mudring, X. Zou, Microporous and Mesoporous Materials, 279 (2019) 400-406.
[63] J. Xue, Y. Wang, G. Yang, Y. Wang, J Rare Earth, (2023).
[64] X. Lu, Y. Tang, G. Yang, Y.-Y. Wang, Journal of Materials Chemistry C, 11 (2023) 2328-2335.
[65] S. Zhang, W. Shi, P. Cheng, Coordination Chemistry Reviews, 352 (2017) 108-150.
[66] S. Zhang, F. Ou, S. Ning, P. Cheng, Inorganic Chemistry Frontiers, 8 (2021) 1865-1899.
[67] A. Verma, S.K.S. Hossain, S.S. Sunkari, J. Reibenspies, S. Saha, New Journal of Chemistry, 45 (2021) 2696-2709.
[68] T.D. Pasatoiu, A.M. Madalan, M.U. Kumke, C. Tiseanu, M. Andruh, Inorganic Chemistry, 49 (2010) 2310-2315.
[69] Y. Cui, B. Chen, G. Qian, Coordination Chemistry Reviews, 273-274 (2014) 76-86.
[70] K.F. Kayani, K.M. Omer, New Journal of Chemistry, 46 (2022) 8152-8161.
[71] Y. Hasegawa, Y. Kitagawa, Journal of Photochemistry and Photobiology C: Photochemistry Reviews, 51 (2022) 100485.
[72] B. Yan, Accounts of Chemical Research, 50 (2017) 2789-2798.
[73] S.S. Skourtis, C. Liu, P. Antoniou, A.M. Virshup, D.N. Beratan, Proceedings of the National Academy of Sciences, 113 (2016) 8115-8120.
[74] S.A. Younis, N. Bhardwaj, S.K. Bhardwaj, K.-H. Kim, A. Deep, Coordination Chemistry Reviews, 429 (2021) 213620.
[75] J. Luo, B.-S. Liu, X.-R. Zhang, R.-T. Liu, J Mol Struct, 1177 (2019) 444-448.
[76] B. Liu, W.-P. Wu, L. Hou, Y.-Y. Wang, Chemical Communications, 50 (2014) 8731-8734.
[77] X.R. Wang, K. Batra, G. Clavier, G. Maurin, B. Ding, A. Tissot, C. Serre, Chemistry-a European Journal, (2023).
[78] X.R. Wang, G. Clavier, Y. Zhang, K. Batra, N.A. Xiao, G. Maurin, B. Ding, A. Tissot, C. Serre, Chemical Science, 14 (2023) 5386-5395.
[79] S. Omagari, T. Nakanishi, Y. Kitagawa, T. Seki, K. Fushimi, H. Ito, A. Meijerink, Y. Hasegawa, Sci Rep-Uk, 6 (2016) 37008.
[80] Y. Zhou, B. Yan, Journal of Materials Chemistry C, 3 (2015) 9353-9358.
[81] H. Yu, Q. Liu, M. Fan, J. Sun, Z.-M. Su, X. Li, X. Wang, Dyes and Pigments, 197 (2022) 109812.
[82] H. Yu, Q. Liu, J. Li, Z.-M. Su, X. Li, X. Wang, J. Sun, C. Zhou, X. Hu, Journal of Materials Chemistry C, 9 (2021) 562-568.
[83] X. Feng, Y. Shang, K. Zhang, M. Hong, J. Li, H. Xu, L. Wang, Z. Li, CrystEngComm, 24 (2022) 4187-4200.
[84] Y. Zhang, H. Lu, B. Yan, Sensors and Actuators B: Chemical, 349 (2021) 130736.
[85] Y. Liu, C. Zhang, C. Xu, C. Lin, K. Sun, J. Wang, X. Chen, L. Li, A.K. Whittaker, H.-B. Xu, Dalton Transactions, 47 (2018) 11253-11263.
[86] X. Zhang, B. Li, H. Ma, L. Zhang, H. Zhao, ACS Applied Materials & Interfaces, 8 (2016) 17389-17394.
[87] Y.-J. Tong, L.-D. Yu, J. Zheng, G. Liu, Y. Ye, S. Huang, G. Chen, H. Yang, C. Wen, S. Wei, J. Xu, F. Zhu, J. Pawliszyn, G. Ouyang, Analytical Chemistry, 92 (2020) 15550-15557.
[88] G. Ji, T. Zheng, X. Gao, Z. Liu, Sensors and Actuators B: Chemical, 284 (2019) 91-95.
[89] Y. Zhang, B. Yan, Nanoscale, 11 (2019) 22946-22953.
[90] X. Zheng, R. Fan, Y. Song, A. Wang, K. Xing, X. Du, P. Wang, Y. Yang, Journal of Materials Chemistry C, 5 (2017) 9943-9951.
[91] Y. Gao, Y. Qi, K. Zhao, Q. Wen, J. Shen, L. Qiu, W. Mou, Sensors and Actuators B: Chemical, 257 (2018) 553-560.
[92] M. Li, Y. Gao, W. Yang, C. Zhang, Y. Fang, C. Wang, S. Song, Q. Pan, Inorganic Chemistry, 61 (2022) 9801-9807.
[93] Y. Zhang, X. Xu, B. Yan, Journal of Materials Chemistry C, 10 (2022) 3576-3584.
[94] X.-C. Sun, Z.-Z. Cong, S.-Y. Wu, Y. Zhang, M.-C. Zhu, X.-J. Bai, Journal of Materials Chemistry C, 10 (2022) 15516-15523.
[95] K. Zheng, Z.-Q. Liu, Y. Huang, F. Chen, C.-H. Zeng, S. Zhong, S.W. Ng, Sensors and Actuators B: Chemical, 257 (2018) 705-713.
[96] L. Yu, L. Feng, L. Xiong, S. Li, Q. Xu, X. Pan, Y. Xiao, ACS Applied Materials & Interfaces, 13 (2021) 11646-11656.
[97] Y. Du, H. Yang, R. Liu, C. Shao, L. Yang, Dalton Transactions, 49 (2020) 13003-13016.
[98] X.-y. Wang, X. Yao, Q. Huang, Y.-x. Li, G.-h. An, G.-m. Li, Analytical Chemistry, 90 (2018) 6675-6682.
[99] P. Zhao, Y. Liu, C. He, C. Duan, Inorganic Chemistry, 61 (2022) 3132-3140.
[100] L. Yu, L. Feng, L. Xiong, S. Li, S. Wang, Z. Wei, Y. Xiao, J Hazard Mater, 434 (2022) 128914.
[101] H.-W. Yang, P. Xu, B. Ding, Z.-Y. Liu, X.-J. Zhao, E.-C. Yang, European Journal of Inorganic Chemistry, 2019 (2019) 5077-5084.
[102] X. Shi, Y. Fan, J. Xu, H. Qi, J. Chai, J. Sun, H. Jin, X. Chen, P. Zhang, L. Wang, Inorg Chim Acta, 483 (2018) 473-479.
[103] X. Dao, Y. Ni, H. Pan, Sensors and Actuators B: Chemical, 271 (2018) 33-43.
[104] Z. Zhou, X. Li, Y. Tang, C.C. Zhang, H. Fu, N. Wu, L. Ma, J. Gao, Q. Wang, Chemical Engineering Journal, 351 (2018) 364-370.
[105] Y.-l. Li, J. Wang, B.-b. Shi, J. Li, Supramol Chem, 28 (2016) 640-646.
[106] X.-Z. Song, Y.-X. Wang, J.-W. Yan, X. Chen, Y.-L. Meng, Z. Tan, Chemistryselect, 3 (2018) 9564-9570.
[107] K. Ge, X. He, Z. Xu, R. Chu, Chemistryselect, 4 (2019) 12573-12579.
[108] J. Liu, L. Pei, Z. Xia, Y. Xu, Crystal Growth & Design, 19 (2019) 6586-6591.
[109] X.-J. Che, S.-L. Hou, Y. Shi, G.-L. Yang, Y.-L. Hou, B. Zhao, Dalton Transactions, 48 (2019) 3453-3458.
[110] J.-J. Pang, Z.-Q. Yao, K. Zhang, Q.-W. Li, Z.-X. Fu, R. Zheng, W. Li, J. Xu, X.-H. Bu, Angewandte Chemie International Edition, 62 (2023) e202217456.
[111] H. Wang, X. Wang, M. Liang, G. Chen, R.-M. Kong, L. Xia, F. Qu, Analytical Chemistry, 92 (2020) 3366-3372.
[112] J. Ren, Z. Niu, Y. Ye, C.-Y. Tsai, S. Liu, Q. Liu, X. Huang, A. Nafady, S. Ma, Angewandte Chemie International Edition, 60 (2021) 23705-23712.
[113] Y. Zhao, M.-Y. Wan, J.-P. Bai, H. Zeng, W. Lu, D. Li, Journal of Materials Chemistry A, 7 (2019) 11127-11133.
[114] L. Pan, X. Huang, J. Li, Y. Wu, N. Zheng, Angew Chem Int Ed Engl, 39 (2000) 527-530.
[115] Y.P. Jiang, X.H. Fang, Q. Wang, J.Z. Huo, Y.Y. Liu, X.R. Wang, B. Ding, Commun Chem, 6 (2023).
[116] S. Omagari, Springer Theses-Reco, (2019) 49-76.
[117] M. Pan, W.M. Liao, S.Y. Yin, S.S. Sun, C.Y. Su, Chemical Reviews, 118 (2018) 8889-8935.

[118] E. Echenique-Errandonea, R.F. Mendes, F. Figueira, D. Choquesillo-Lazarte, G. Beobide, J. Cepeda, D. Ananias, A. Rodriguez-Dieguez, F.A.A. Paz, J.M. Seco, Inorganic Chemistry, 61 (2022) 12977-12990.
[119] Y. Pan, H.Q. Su, E.L. Zhou, H.Z. Yin, K.Z. Shao, Z.M. Su, Dalton Transactions, 48 (2019) 3723-3729.
[120] X.M. Luo, X.X. He, J. Shi, C.H. Cui, Y. Xu, Zeitschrift Fur Anorganische Und Allgemeine Chemie, 644 (2018) 43-49.
[121] H.Z. Wang, D. Zhao, Y.J. Cui, Y. Yang, G.D. Qian, Journal of Solid State Chemistry, 246 (2017) 341-345.
[122] C. Serre, F. Millange, C. Thouvenot, N. Gardant, F. Pellé, G. Férey, Journal of Materials Chemistry, 14 (2004) 1540-1543.
[123] H.S. Jena, A.M. Kaczmarek, C. Krishnaraj, X. Feng, K. Vijayvergia, H. Yildirim, S.N. Zhao, R. Van Deun, P. Van Der Voort, Crystal Growth & Design, 19 (2019) 6339-6350.
[124] P. Silva, F. Vieira, A.C. Gomes, D. Ananias, J.A. Fernandes, S.M. Bruno, R. Soares, A.A. Valente, J. Rocha, F.A.A. Paz, Journal of the American Chemical Society, 133 (2011) 15120-15138.
[125] T. Xian, Q. Meng, F.R. Gao, M. Hu, X.H. Wang, Coordination Chemistry Reviews, 474 (2023).
[126] Z.Q. Zhao, L. Liu, J. Chen, P.F. Wang, X.Y. Wu, Y.H. Zhang, Y.H. Wu, Z. Zhao, F.N. Shi, J Alloy Compd, 938 (2023).
[127] B. Li, J.P. Dong, Z. Zhou, R. Wang, L.Y. Wang, S.Q. Zang, Journal of Materials Chemistry C, 9 (2021) 3429-3439.
[128] Z.J. Zhang, L.P. Liu, T. Zhang, H.X. Tang, Acs Applied Materials & Interfaces, 15 (2023) 18982-18991.
[129] Z.-P. Dong, F. Zhao, L. Zhang, Z.-L. Liu, Y.-Q. Wang, New Journal of Chemistry, 44 (2020) 10239-10249.
[130] X. Zeng, Z. Long, X. Jiang, Y. Zhang, Q. Liu, J. Hu, C. Li, L. Wu, X. Hou, Analytical Chemistry, 92 (2020) 5500-5508.
[131] D.B. Kanzariya, M.Y. Chaudhary, T.K. Pal, Dalton Transactions, 52 (2023) 7383-7404.
[132] T.T. Feng, Y.X. Ye, X. Liu, H. Cui, Z.Q. Li, Y. Zhang, B. Liang, H.R. Li, B.L. Chen, Angewandte Chemie-International Edition, 59 (2020) 21752-21757.
[133] J.F. Feng, S.Y. Gao, T.F. Liu, J.L. Shi, R. Cao, Acs Applied Materials & Interfaces, 10 (2018) 6014-6023.
[134] Y. Yang, L. Chen, F.L. Jiang, M.X. Yu, X.Y. Wan, B. Zhang, M.C. Hong, Journal of Materials Chemistry C, 5 (2017) 1981-1989.
[135] C. Viravaux, O. Oms, A. Dolbecq, E. Nassar, L. Busson, C. Mellot-Draznieks, R. Dessapt, H. Serier-Brault, P. Mialane, Journal of Materials Chemistry C, 9 (2021) 8323-8328.
[136] F. Vanden Bussche, A.M. Kaczmarek, V. Van Speybroeck, P. Van Der Voort, C.V. Stevens, Chemistry-a European Journal, 27 (2021) 7214-7230.
[137] J. Bi, M. Fang, J. Wang, S. Xia, Y. Zhang, J. Zhang, G. Vegesna, S. Zhang, M. Tanasova, F.-T. Luo, H. Liu, Inorg Chim Acta, 468 (2017) 140-145.
[138] X. Lian, D. Zhao, Y. Cui, Y. Yang, G. Qian, Chemical Communications, 51 (2015) 17676-17679.
[139] D. Zhao, X. Han, S. Wang, J. Liu, Y. Lu, C. Li, Chemistry – A European Journal, 26 (2020) 3145-3151.
[140] X.Z. Wang, X.R. Wang, Y.Y. Liu, J.Z. Huo, Y. Li, Q. Wang, K. Liu, B. Ding, Ultrasonics Sonochemistry, 59 (2019) 104734.
[141] X. Zeng, Y. Zhang, J. Zhang, H. Hu, X. Wu, Z. Long, X. Hou, Microchem J, 134 (2017) 140-145.
[142] Y. Su, J. Yu, Y. Li, S.F.Z. Phua, G. Liu, W.Q. Lim, X. Yang, R. Ganguly, C. Dang, C. Yang, Y. Zhao, Commun Chem, 1 (2018) 12.
[143] D.-M. Chen, C.-X. Sun, Y. Peng, N.-N. Zhang, H.-H. Si, C.-S. Liu, M. Du, Sensors and Actuators B: Chemical, 265 (2018) 104-109.
[144] Y.-P. Wu, G.-W. Xu, W.-W. Dong, J. Zhao, D.-S. Li, J. Zhang, X. Bu, Inorganic Chemistry, 56 (2017) 1402-1411.
[145] H. Min, Z. Chen, Z. Han, K. Wang, J. Xu, W. Shi, P. Cheng, Commun Chem, 5 (2022) 74.
[146] S. Wu, Y. Lin, J. Liu, W. Shi, G. Yang, P. Cheng, Advanced Functional Materials, 28 (2018) 1707169.
[147] B. Li, W. Wang, Z. Hong, E.-S.M. El-Sayed, D. Yuan, Chemical Communications, 55 (2019) 6926-6929.
[148] W. Yan, C. Zhang, S. Chen, L. Han, H. Zheng, ACS Applied Materials & Interfaces, 9 (2017) 1629-1634.
[149] Z. Zhang, L. Wang, G. Li, B. Ye, Analyst, 142 (2017) 1821-1826.
[150] H.-Q. Yin, X.-Y. Wang, X.-B. Yin, Journal of the American Chemical Society, 141 (2019) 15166-15173.
[151] J. Yin, H. Chu, S. Qin, H. Qi, M. Hu, Sensors-Basel, 21 (2021) 7355.
[152] R.-C. Gao, F.-S. Guo, N.-N. Bai, Y.-L. Wu, F. Yang, J.-Y. Liang, Z.-J. Li, Y.-Y. Wang, Inorganic Chemistry, 55 (2016) 11323-11330.
[153] X. Li, S. Zhou, S. Lu, D. Tu, W. Zheng, Y. Liu, R. Li, X. Chen, ACS Applied Materials & Interfaces, 11 (2019) 43989-43995.
[154] Y. Zhou, B. Yan, Chemical Communications, 52 (2016) 2265-2268.
[155] X. Lian, B. Yan, Rsc Adv, 6 (2016) 11570-11576.
[156] Y. Zhang, B. Li, H. Ma, L. Zhang, H. Jiang, H. Song, L. Zhang, Y. Luo, Journal of Materials Chemistry C, 4 (2016) 7294-7301.
[157] L. Bourda, A.M. Kaczmarek, M. Peng, S. Mohanty, H. Rijckaert, P. Van Der Voort, K. Van Hecke, Acs Applied Materials & Interfaces, 15 (2023) 37696-37705.
[158] H.S. Jena, H. Rijckaert, C. Krishnaraj, I. Van Driessche, P. Van der Voort, A.M. Kaczmarek, Chemistry of Materials, 33 (2021) 8007-8017.
[159] M. Safdar, A. Ghazy, M. Lastusaari, M. Karppinen, Journal of Materials Chemistry C, 8 (2020) 6946-6965.
[160] Y.H. Feng, X.J. Li, S. Lu, R.F. Li, Z.L. Gong, X.Y. Shang, Y.F. Pei, W. Zheng, D.T. Tu, X.Y. Chen, Nano Research, 16 (2023) 1482-1490.
[161] Y.Q. Li, Y.H. Yang, X.L. Guo, Y.L. Chen, Z.H. Wang, L.L. Hu, W. Wu, J.K. Zhu, Acs Applied Nano Materials, 6 (2023).
[162] L.M. Zhao, C. Redshaw, K.X. Ding, P.Y. Zhang, B. Chen, Z.R. Chen, J.G. Hu, H.H. Li, Applied Surface Science, 614 (2023).
[163] Z.H. Pan, Z.Z. Weng, X.J. Kong, L.S. Long, L.S. Zheng, Coordination Chemistry Reviews, 457 (2022).
[164] Y.J. Tong, L.D. Yu, N. Li, M.H. Shen, X.R. Peng, H.S. Yang, Y.X. Ye, F. Zhu, J. Pawliszyn, J.Q. Xu, G.F. Ouyang, Chemical Science, 13 (2022) 13948-13955.
[165] X.H. Wei, G.D. Zhao, P.F. Feng, Y. Kou, Y. Tang, Acs Applied Nano Materials, 5 (2022) 1161-1168.
[166] X. Fang, X.Y. Wang, Y.X. Li, Q.J. Li, S. Mao, Analytical Chemistry, (2023).
[167] X.C. Fu, B.W. Ding, D. D'Alessandro, Coordination Chemistry Reviews, 475 (2023).
[168] Y.M. Jo, Y.K. Jo, J.H. Lee, H.W. Jang, I.S. Hwang, D. Yoo, Advanced Materials, (2023).
[169] K.K. Ma, Y.H. Cheung, K.O. Kirlikovali, X.L. Wang, T. Islamoglu, J.H. Xin, O.K. Farha, Accounts Mater Res, 4 (2023) 168-179.
[170] J. Qin, J.J. Li, H.S. Zeng, J. Tang, D.P. Tang, Analyst, 148 (2023) 2200-2213.
[171] J.M. Xu, J. Ma, Y. Peng, S. Cao, S.T. Zhang, H. Pang, Chinese Chem Lett, 34 (2023).
[172] X.-L. Xue, Y. Wang, S. Chen, K.-P. Wang, S.-Y. Niu, Q.-S. Zong, Y. Jiang, Z.-Q. Hu, Spectrochimica Acta Part A: Molecular and Biomolecular Spectroscopy, 284 (2023) 121778.
[173] Y.F. Shi, Y.P. Jiang, X.Z. Wang, Z.Q. Zhang, J.Z. Huo, Y.Y. Liu, X.R. Wang, B. Ding, ACS Applied Nano Materials, 5 (2022) 15629-15641.
[174] S. Zhu, Y. Song, X. Zhao, J. Shao, J. Zhang, B. Yang, Nano Research, 8 (2015) 355-381.
[175] Y. Wang, Z.G. Song, J.W. Wan, S. Betzler, Y.J. Xie, C. Ophus, K.C. Bustillo, P. Ercius, L.W. Wang, H.M. Zheng, Journal of the American Chemical Society, 144 (2022) 23474-23482.
[176] Y.B. An, D.Z. Xu, X.F. Wen, C. Chen, G. Liu, Z.X. Lu, Advanced Healthcare Materials, (2023).
[177] C.D.S. Brites, R. Marin, M. Suta, A.C.N. Neto, E. Ximendes, D. Jaque, L.D. Carlos, Advanced Materials, (2023).
[178] R.J. Chen, Z.B. Wang, T. Pang, Q. Teng, C.H. Li, N.Z. Jiang, S. Zheng, R.D. Zhang, Y.H. Zheng, D.Q. Chen, F.L. Yuan, Advanced Materials, (2023).
[179] Y.X. Shang, H.M. Sun, R.Y. Yu, F.D. Zhang, X.Y. Liang, H.L. Li, J.W. Li, Z.F. Yan, T. Zeng, X. Chen, J.B. Zeng, Environ Sci Technol, 57 (2023) 11231-11240.
[180] R. Ghasemzadeh, K. Akhbari, Crystal Growth & Design, (2023).
[181] D. Buso, J. Jasieniak, M.D.H. Lay, P. Schiavuta, P. Scopece, J. Laird, H. Amenitsch, A.J. Hill, P. Falcaro, Small, 8 (2012) 80-88.
[182] J. Qin, B. Liu, K.-H. Lam, S. Song, X. Li, X. Hu, ACS Sustainable Chemistry & Engineering, 8 (2020) 17791-17799.
[183] Y. Dong, J. Cai, Q. Fang, X. You, Y. Chi, Analytical Chemistry, 88 (2016) 1748-1752.
[184] A. Abdelhafiz, A.N.M. Tanvir, M.X. Zeng, B.M. Wang, Z.C. Ren, A.R. Harutyunyan, Y.L. Zhang, J. Li, Advanced Science, 10 (2023).
[185] W. Ahmad, H. Jeong, H.H. Nahm, Y. Lee, E. Park, H. Lee, G. Ali, Y.H. Kim, J. Jurng, Y. Oh, Chemical Engineering Journal, 467 (2023).
[186] Y. Akinaga, T. Kawawaki, H. Kameko, Y. Yamazaki, K. Yamazaki, Y. Nakayasu, K. Kato, Y. Tanaka, A.T. Hanindriyo, M. Takagi, T. Shimazaki, M. Tachikawa, A. Yamakata, Y. Negishi, Advanced Functional Materials, (2023).

[187] X. Dai, X.H. Liu, T. Xu, C.J. Gu, F.Y. Zhao, T. Jiang, Sensors and Actuators B-Chemical, 386 (2023).
[188] J.Y. Zhang, S. Bhattacharya, A.B. Muller, L. Kiss, C. Silvestru, N. Kuhnert, U. Kortz, Chemical Communications, 59 (2023) 5918-5921.
[189] A. Beck, H. Frey, X. Huang, A.H. Clark, E.D. Goodman, M. Cargnello, M. Willinger, J.A. van Bokhoven, Angewandte Chemie-International Edition, (2023).
[190] Z.Y. Yang, T.T. Zhao, S.Y. Hao, R.T. Wang, C.Y. Zhu, Y.X. Tang, C. Guo, J.R. Liu, X.D. Wen, F.L. Wang, Advanced Science, 10 (2023).
[191] F. Qu, Y. Ding, X. Lv, L. Xia, J. You, W. Han, Anal Bioanal Chem, 411 (2019) 3979-3988.
[192] Z.J. Zhang, Y.X. Ye, S.C. Xiang, B.L. Chen, Accounts of Chemical Research, 55 (2022) 3752-3766.
[193] J. Fonseca, L.X. Meng, I. Imaz, D. Maspoch, Chemical Society Reviews, 52 (2023) 2528-2543.
[194] Y. Ben, C. Fu, M. Hu, L. Liu, M.H. Wong, C. Zheng, Environmental Research, 169 (2019) 483-493.
[195] Z.S. Han, K.Y. Wang, H.C. Zhou, P. Cheng, W. Shi, Nat Protoc, 18 (2023) 1621-+.
[196] B. Lalchawimawia, A. Sil, T. Banerjee, N. Singh, A. Bhatnagar, R. Mukhopadhyay, A. Mandal, Coordination Chemistry Reviews, 490 (2023).
[197] X.J. Ma, Q. Ou, J.J. Yuan, J.J. Yang, S.X. Xu, X.F. Zhang, Chemical Engineering Journal, 464 (2023).
[198] H.J. Zhu, B.X. Liu, M.Z. Wang, J.M. Pan, L.Z. Xu, P.W. Hu, X.H. Niu, Analytical Chemistry, 95 (2023) 4776-4785.
[199] R. Xue, Y.S. Liu, S.L. Huang, G.Y. Yang, Acs Sensors, 8 (2023) 2124-2148.
[200] C. Li, C. Zeng, Z. Chen, Y. Jiang, H. Yao, Y. Yang, W.-T. Wong, J Hazard Mater, 384 (2020) 121498.
[201] S.Y. Wu, Y.N. Lin, J.W. Liu, W. Shi, G.M. Yang, P. Cheng, Advanced Functional Materials, 28 (2018).
[202] B. Yan, Journal of Materials Chemistry C, 7 (2019) 8155-8175.
[203] H.W. Yang, P. Xu, B. Ding, X.G. Wang, Z.Y. Liu, H.K. Zhao, X.J. Zhao, E.C. Yang, Crystal Growth & Design, 20 (2020) 7615-7625.
[204] Y.S. Jiang, Y.T. Huang, X.X. Shi, Z.J. Lu, J.M. Ren, Z.M. Wang, J.N. Xu, Y. Fan, L. Wang, Inorganic Chemistry Frontiers, 8 (2021) 4924-4932.
[205] Z.Q. Tan, Y. Quan, Y.F. Li, T. Yang, X.H. Zhou, Y.J. You, Chinese Journal of Chemistry, 41 (2023) 265-272.
[206] X. Xu, M.Y. Ma, T.X. Sun, X. Zhao, L. Zhang, Biosensors-Basel, 13 (2023).
[207] A. Anwar, M. Imran, H.M.N. Iqbal, Coordination Chemistry Reviews, 493 (2023).
[208] Z. Fredj, B. Singh, M. Bahri, P.W. Qin, M. Sawan, Chemosensors, 11 (2023).
[209] C. Zhan, J. Cheng, B. Li, S. Huang, F. Zeng, S. Wu, Analytical Chemistry, 90 (2018) 8807-8815.
[210] L. Yu, Z. Gao, Q. Xu, X. Pan, Y. Xiao, Biosens Bioelectron, 210 (2022) 114320.
[211] S.N. Zhao, L.J. Li, X.Z. Song, M. Zhu, Z.M. Hao, X. Meng, L.L. Wu, J. Feng, S.Y. Song, C. Wang, H.J. Zhang, Advanced Functional Materials, 25 (2015) 1463-1469.
[212] H.R. Guan, M.X. Qi, L.F. Shi, W.S. Liu, L.Z. Yang, W. Dou, Acs Applied Materials & Interfaces, 15 (2023) 18114-18124.
[213] R. Jankowski, M. Wyczesany, S. Chorazy, Chemical Communications, 59 (2023).
[214] Z.J. Li, Q. Wang, K.L. Yu, W.L. Cui, Y.B. He, B.L. Chen, D. Zhao, Inorganic Chemistry, 62 (2023) 5652-5659.
[215] S.Y. Liu, W. Liu, Y.L. Sun, W.S. Liu, Inorganic Chemistry, 62 (2023) 9781-9791.
[216] H.L. Guo, Y.Z. Zhu, S.L. Qiu, J.A. Lercher, H.J. Zhang, Advanced Materials, 22 (2010) 4190-+.
[217] X. Yang, H. Zou, X. Sun, T. Sun, C. Guo, Y. Fu, C.-M.L. Wu, X. Qiao, F. Wang, Advanced Optical Materials, 7 (2019) 1900336.
[218] A. Halder, D.C. Bain, J. Oktawiec, M.A. Addicoat, S. Tsangari, J.J.F. -Rivera, T.A. Pitt, A.J. Musser, P.J. Milner, Journal of the American Chemical Society, 145 (2023) 1072-1082.
[219] X. Zhang, D.Y. Liu, J.H. Yu, X. Li, H.W. Zheng, Y.N. Zhou, C.Y. Huang, Y.Y. Zhu, C.Q. Jiao, Z.G. Sun, Dalton Transactions, 52 (2023) 8558-8566.
[220] X.X. Zhang, D.G. Cai, Y.P. Li, Y.Q. Chen, S.J. Liu, Crystal Growth & Design, (2023).
[221] Y. Zhang, Y.H. Liu, P.G. Karmaker, L.L. Zhang, K.J. Yang, L.F. Chen, X.P. Yang, Acs Applied Materials & Interfaces, (2023).
[222] Y. Zhang, X.Y. Yuan, X.C. Zhu, D.W. Zhang, H.L. Liu, B.G. Sun, Anal Chim Acta, 1239 (2023).
[223] Z. Zhang, J. Zhou, X. Chen, F. Fang, S.Y. Wang, S.S. Zhang, L. Du, Q.H. Zhao, Inorganic Chemistry, (2023).
[224] Y.K. Yang, X.X. Zeng, Y. Tian, X.M. Wang, X. Jing, L.G. Yu, B.Q. Bai, J.H. Zhang, S. Qin, Food Chem, 422 (2023).
[225] L. Yu, X. Li, Y.F. Lu, P.C. Su, M. Yuan, Q. Zhang, L.X. Wang, D.G. Wang, M.T. Sun, S.H. Wang, Sensors and Actuators B-Chemical, 385 (2023).
[226] L.D. Zhang, X.L. Wang, W.H. Kong, Y. Zhao, L. Xia, F.L. Qu, Sensors and Actuators B-Chemical, 386 (2023).
[227] P.P. Zhang, A.Y. Ni, J.J. Zhang, B.L. Zhang, H.A. Zhou, H. Zhao, S.Q. Liu, J. Ni, C.Y. Duan, Sensors and Actuators B-Chemical, 384 (2023).
[228] P. Li, L. Zhang, S. Zhang, C. Xu, Y. Li, J. Qu, S. Li, G. Mao, H. Wang, Journal of Materials Chemistry B, 9 (2021) 5998-6005.
[229] R. Xie, P. Yang, J. Liu, X. Zou, Y. Tan, X. Wang, J. Tao, P. Zhao, Talanta, 231 (2021) 122366.
[230] H.-Y. Li, Y.-L. Wei, X.-Y. Dong, S.-Q. Zang, T.C.W. Mak, Chemistry of Materials, 27 (2015) 1327-1331.
[231] C. Li, C. Zeng, Z. Chen, Y. Jiang, H. Yao, Y. Yang, W.T. Wong, J Hazard Mater, 384 (2020) 121498.
[232] Y. Gao, G. Yu, K. Liu, B. Wang, Sensors and Actuators B: Chemical, 257 (2018) 931-935.
[233] B. Wang, B. Yan, Talanta, 208 (2020) 120438.
[234] L. Zhao, M. Wang, X. Song, X. Liu, H. Ju, H. Ai, Q. Wei, D. Wu, Chemical Engineering Journal, 434 (2022) 134691.
[235] C. Ji, R. Fan, J. Zhang, T. Sun, K. Zhu, X. Jiang, W. Jia, Y. Yang, Sensors and Actuators B: Chemical, 357 (2022) 131399.
[236] J.-N. Hao, B. Yan, Advanced Functional Materials, 27 (2017) 1603856.
[237] C. Viravaux, O. Oms, A. Dolbecq, E. Nassar, L. Busson, C. Mellot-Draznieks, R. Dessapt, H. Serier-Brault, P. Mialane, Journal of Materials Chemistry C, 9 (2021) 8323-8328.
[238] J.-f. Feng, T.-f. Liu, J. Shi, S.-y. Gao, R. Cao, ACS Applied Materials & Interfaces, 10 (2018) 20854-20861.
[239] J. Zhang, G. Shi, Anal Chim Acta, 1198 (2022) 339572.
[240] Y. Wang, J. He, M. Zheng, M. Qin, W. Wei, Talanta, 191 (2019) 519-525.
[241] R. Jalili, A. Khataee, M.-R. Rashidi, R. Luque, Sensors and Actuators B: Chemical, 297 (2019) 126775.
[242] G.W. Xu, Y.P. Wu, W.W. Dong, J. Zhao, X.Q. Wu, D.S. Li, Q. Zhang, Small, 13 (2017).
[243] Q. Liu, H. Wang, P. Han, X. Feng, Analyst, 144 (2019) 6025-6032.
[244] C. Sun, S. Zhao, F. Qu, W. Han, J. You, Microchim Acta, 187 (2019) 34.
[245] A. Afzalinia, M. Mirzaee, ACS Applied Materials & Interfaces, 12 (2020) 16076-16087.
[246] S.Z. Du, Z. Sun, L. Han, M. Qing, H.Q. Luo, N.B. Li, Sensors and Actuators B: Chemical, 324 (2020) 128757.
[247] K. Yin, S. Wu, H. Zheng, L. Gao, J. Liu, C. Yang, L.-W. Qi, J. Peng, Langmuir, 37 (2021) 5321-5328.
[248] Z. Sun, Y.Z. Fan, S.Z. Du, Y.Z. Yang, Y. Ling, N.B. Li, H.Q. Luo, Analytical Chemistry, 92 (2020) 7273-7281.
[249] Y. Lv, X. Tian, Y. Li, Y. Nie, Sensors and Actuators B: Chemical, 372 (2022) 132641.
[250] X. Liu, J. Zhang, Y. Ma, D. Zhao, D. Huo, H. Luo, J. Li, X. Luo, C. Hou, Anal Methods-Uk, 14 (2022) 1585-1593.
[251] L. Li, J.-Y. Zou, S.-Y. You, H.-M. Cui, G.-P. Zeng, J.-Z. Cui, Dalton Transactions, 46 (2017) 16432-16438.
[252] X. Wang, C. Chu, Y. Wu, Y. Deng, J. Zhou, M. Yang, S. Zhang, D. Huo, C. Hou, Sensors and Actuators B: Chemical, 321 (2020) 128455.
[253] Z. Qi, Y. Chen, Biosensors and Bioelectronics, 87 (2017) 236-241.
[254] X. Zhang, K. Jiang, H. He, D. Yue, D. Zhao, Y. Cui, Y. Yang, G. Qian, Sensors and Actuators B: Chemical, 254 (2018) 1069-1077.
[255] S.-Z. Huang, S.-S. Liu, H.-j. Zhang, Z. Han, G. Zhao, X.-Y. Dong, S.-Q. Zang, ACS Applied Materials & Interfaces, 12 (2020) 28720-28726.
[256] X. Zeng, J. Hu, M. Zhang, F. Wang, L. Wu, X. Hou, Analytical Chemistry, 92 (2020) 2097-2102.
[257] E. Gao, S. Wu, J. Wang, M. Zhu, Y. Zhang, V.P. Fedin, Advanced Optical Materials, 8 (2020) 1901659.
[258] T. Sun, R. Fan, R. Xiao, T. Xing, M. Qin, Y. Liu, S. Hao, W. Chen, Y. Yang, Journal of Materials Chemistry A, 8 (2020) 5587-5594.